Microsc. Microanal. 11, 378–400, 2005
DOI: 10.1017/S1431927605050361

Microscopy AND Microanalysis

Recent Advances in Electron Tomography: TEM and HAADF-STEM Tomography for Materials Science and Semiconductor Applications

Christian Kübel,[1]* Andreas Voigt,[1] Remco Schoenmakers,[1] Max Otten,[1] David Su,[2] Tan-Chen Lee,[2] Anna Carlsson,[3] and John Bradley[4]

[1]*FEI Company, Applications Laboratory, Achtseweg Noord 5, 5651GG Eindhoven, The Netherlands*
[2]*Taiwan Semiconductor Manufacturing Company, Ltd., Failure Analysis Division 9, Creation Road 1, Science-Based Industrial Park Hsin-Chu, Taiwan, Republic of China*
[3]*Haldor Topsøe A/S, Environmental and Materials Department, Research and Development, Nymøllevej 55, DK-2800 Lyngby, Denmark*
[4]*Institute for Geophysics and Planetary Physics, Lawrence Livermore National Laboratory, MS L-413, Livermore, CA 94550, USA*

Abstract: Electron tomography is a well-established technique for three-dimensional structure determination of (almost) amorphous specimens in life sciences applications. With the recent advances in nanotechnology and the semiconductor industry, there is also an increasing need for high-resolution three-dimensional (3D) structural information in physical sciences. In this article, we evaluate the capabilities and limitations of transmission electron microscopy (TEM) and high-angle-annular-dark-field scanning transmission electron microscopy (HAADF-STEM) tomography for the 3D structural characterization of partially crystalline to highly crystalline materials. Our analysis of catalysts, a hydrogen storage material, and different semiconductor devices shows that features with a diameter as small as 1–2 nm can be resolved in three dimensions by electron tomography. For partially crystalline materials with small single crystalline domains, bright-field TEM tomography provides reliable 3D structural information. HAADF-STEM tomography is more versatile and can also be used for high-resolution 3D imaging of highly crystalline materials such as semiconductor devices.

Key words: 3D imaging, electron tomography, transmission electron microscopy (TEM), high-angle-annular-dark-field scanning transmission electron microscopy (HAADF-STEM), semiconductor devices, catalyst

Introduction

Both the characteristic dimensions of semiconductor devices and the feature size in nanostructured materials are decreasing with recent advances in nanotechnology and semiconductor manufacturing. This trend results in improved CPU performance and higher storage capacities, but also in new materials such as catalysts with improved efficiencies (Breysse et al., 2003; Dhar et al., 2003). However, the smaller dimensions in these new materials also present new challenges for materials characterization and defect analysis, including three-dimensional (3D) metrology, surface roughness measurements, characterization of buried defects, and simple understanding of complex 3D geometries.

Received April 1, 2004; accepted February 15, 2005.
Christian Kübel is now at Fraunhofer Institut für Fertigungstechnik und Angewandte Materialforschung, Wiener Straße 12, 28359 Bremen, Germany.
*Corresponding author. E-mail: ck@ifam.fraunhofer.de

High-resolution transmission electron microscopy (HRTEM) and scanning transmission electron microscopy (STEM) techniques are routinely used to image materials with atomic resolution (James & Browning, 1999; Browning & Pennycook, 2000; Kisielowski et al., 2001; Spence, 2002, Voyles et al., 2002; Jia et al., 2003). In addition, the combination with energy dispersive X-ray (EDX) and electron energy loss spectroscopy (EELS) techniques provides chemical information on a (sub)nanometer length scale (Batson, 1999; Muller et al., 1999). However, as the feature sizes approach or become smaller than the finite thickness of typical TEM specimens, the limitations of two-dimensional (2D) methods for the analysis of inherently 3D samples become apparent. When different features are projected on top of each other, the results of traditional imaging and analytical techniques cannot be interpreted easily. This makes accurate measurements for metrology difficult (Lee et al., 2002; Zschech et al., 2003) and even means that some defects or small particles might not be visible in traditional 2D projections. To overcome these problems, 3D imaging

(and analytical) techniques are needed to characterize complex nanostructures (de Jong & Koster, 2002; Weyland, 2002; Datye, 2003; Zschech et al., 2003; Anderson et al., 2004; Ziese et al., 2004).

In this article, we evaluate the use of different imaging techniques for electron tomography in order to develop methods to characterize the 3D structure of a wide range of materials. We focus on the 3D characterization of a variety of different materials by bright-field transmission electron microscopy (BF-TEM) and high-angle-annular-dark-field scanning transmission electron microscopy (HAADF-STEM) tomography. Although electron tomography has mainly been used for (almost) amorphous or weakly scattering crystalline materials, here we discuss the benefits and limitations of both methods for materials ranging from partially to highly crystalline.

Electron Tomography

Electron tomography is a technique providing nanometer-scale resolution in three dimensions. Researchers in life sciences have been using BF-TEM tomography for more than a decade to obtain 3D information on biological structures ranging from complete cells to protein complexes (Frank, 1992; Baumeister et al., 1999; McEwen & Marko, 2001; McIntosh, 2001; Koster & Klumperman, 2003; Sali et al., 2003). The 3D structural information is reconstructed digitally from a tilt series of 2D projections, where 50–150 images are acquired by tilting the sample to cover a total tilt range of about $\pm 70^\circ$ while simultaneously correcting for image shift and focus changes. The tilt-series is then processed off-line using backprojection techniques to reconstruct the "original" 3D structure (Frank, 1992).

In addition to life sciences, electron tomography has recently been used to characterize the 3D structure of a variety of different materials (Koster et al., 2000; Buseck et al., 2001; Weyland et al., 2001; Janssen et al., 2001, 2002, 2003; Midgley & Weyland, 2003). However, for materials science applications, care has to be taken that all micrographs in the tilt series fulfill the projection criterion. This criterion states that in order to be suitable for tomography, the micrographs have to be true projections of the structure to be reconstructed. At the very least, this implies that the recorded signal must vary strictly monotonically with (mass) thickness. This projection requirement is met for BF-TEM micrographs of amorphous materials, where mass thickness is the dominant contrast mechanism (with small nonmonotonic contributions due to defocus effects, e.g., Fresnel fringes). Moreover, BF-TEM tomography has been shown to be a powerful technique to study mesopores and the location of metal particles in both zeolites and ordered mesoporous catalyst material (Koster et al., 2000; Janssen et al., 2002, 2003; Ziese et al., 2004). However, the projection criterion is not fulfilled for BF-TEM images of strongly scattering crystalline materials, where diffraction contrast typically dominates the image formation. Therefore, it has been assumed that BF-TEM tomography is of only limited value for these materials.

Other imaging techniques are needed as a general solution for the 3D characterization of (crystalline) materials by electron tomography. These imaging techniques must strongly reduce diffraction effects and fulfill the projection criterion even in the presence of highly crystalline materials. In principle, energy-filtered TEM (EFTEM) and HAADF-STEM imaging are two such alternative techniques. The contrast observed in background-subtracted energy-loss (EFTEM) images of thin samples is, to a first approximation, a function of the projected amount of an atomic species in a specimen. However, diffraction effects also affect the inelastically scattered electrons and induce some diffraction contribution in the elemental maps. More importantly, the elemental maps exhibit a monotonic thickness behavior only for thin samples, whereas the signal decreases drastically for thicker materials. This limits the application of EFTEM tomography (Möbus et al., 2003) to a thickness of less than about 0.7λ (inelastic mean free path) at the maximum tilt angle (Weyland & Midgley, 2003). For example, for a $\pm 65^\circ$ tilt series of a carbonous sample imaged at 200 kV, this limits the thickness to about 35 nm. For materials with a higher density, the thickness is even more limited, which makes this technique unsuitable for typical ultra-microtomed or focused ion beam (FIB) prepared samples in medium voltage (200–400 kV) TEMs.

However, HAADF-STEM imaging does not suffer from the same limitations and potentially provides a more general solution for electron tomography of crystalline materials. As a first approximation, HAADF-STEM imaging results in Z-contrast images due to Rutherford scattering, where the intensity is a function of the atomic number ($Z^{\sim 1.7}$) and is a linear function of the projected sample thickness. In all practical applications, the collection angle is limited, resulting in a small diffraction contribution to the HAADF signal, which is typically negligible for collection angles higher than 70 mrad at 200 kV. The only visible artifacts in HAADF-STEM tilt series are due to channeling effects when a crystal is imaged exactly along a major zone axis. However, as the major zone axes are encountered only rarely during a tilt series, the overall effect on the 3D reconstruction is small, even for highly crystalline materials.

In this article, we present our evaluation of BF-TEM and HAADF-STEM electron tomography for various types of applications. In determining which technique to use, the reliability of the 3D reconstruction (despite slight deviations from the projection criterion) was the most crucial aspect. In addition, we considered the kind of features that can be resolved for materials in three dimensions (resolution) together with practical considerations such as ease of use and time to results. These practical considerations will also help to determine which application fields will potentially benefit from electron tomography. For this overview, we have been looking at three different types of materials: catalysts, a hydrogen storage material, and semiconductor

devices. These samples allow us to cover the range from nanocrystalline materials with high defect densities to highly crystalline devices with single-crystalline domains on the order of 100–500 nm. We did not consider EFTEM tomography due to the strong sample thickness restrictions, but we will discuss the advantages of BF-TEM and HAADF-STEM tomography for the different materials and illustrate what information can be obtained.

Methods

Tomographic Data Acquisition

Single-axis tilt series for BF-TEM tomography were acquired automatically for samples with a thickness of 150–400 nm on a FEI Tecnai Sphera (T20 Twin) using the FEI XPlore3D Tomography Suite. The microscope was operated in TEM mode with parallel illumination under semi-low-dose conditions;† no objective aperture was used to minimize the influence of diffraction effects and the defocus was set to -1 to -2 μm, depending on the magnification, corresponding to a nominal resolution of 1.5 to 2.2 nm at the first crossover in the phase contrast transfer function (CTF). The TEM projections were acquired on a bottom-mounted slow scan CCD camera with 1024 $\times$ 1024 pixels (Gatan 794). Typically 131 electron micrographs were collected over an angular range of $\pm 65°$ in 1° steps. Recentering and refocusing of the area of interest after tilting were done automatically by combining precalibration of the goniometer movements (Ziese et al., 2002*a*) with active shift and focus measurements as implemented in the XPlore3D acquisition software. Typically, the focus measurement was done every 5–10 tilt increments using the beam-tilt-induced image shift (Koster et al., 1987) and the sample shift was measured by comparing the images that were acquired during the tilt series itself. The sample movement was corrected automatically using image/beam shifts and defocus. In addition to the automatic corrections, the user can also manually focus or recenter the area of interest at any time during the acquisition. The total acquisition time for a BF-TEM tomography tilt series was approximately 30–45 min.

Single-axis tilt series for HAADF-STEM tomography were acquired automatically on a Tecnai F20 ST using the XPlore3D 2.0 Tomography Suite. The microscope was operated in HAADF-STEM mode with a nominal spot size of 0.2 nm. A small camera length of 70–100 mm (corresponding to a minimum scattering angle of 50–70 mrad) was used for the HAADF-STEM signal collection to efficiently minimize diffraction effects. Scanned images with 1024 $\times$ 1024 or 2048 $\times$ 2048 pixels were acquired using a frame time of 15–30 s. Typically 71 electron micrographs were collected over an angular range of $\pm 70°$ in 2° steps. Again, recentering and refocusing were done automatically. Typically, the active focus measurement was done every two to three tilt increments based on an automatic analysis of a small HAADF-STEM through-focus series. The focus was adjusted automatically during the acquisition of each frame to compensate for the tilt-induced differences in the height of a planar sample, which otherwise would result in defocus differences across the field of view (dynamic focus). The active shift correction was done based on the acquired tilt series. The total acquisition time for such a HAADF-STEM tilt series is about 45–90 min.

Image Processing

After acquisition, the tilt-series data are transferred to an off-line computer for image processing and reconstruction. We were using IMOD Version 2.7 (by David Mastronarde, James Kremer, and Rick Gaudette at the Boulder Laboratory for 3-Dimensional Electron Microscopy of Cells) and our own Inspect3D Version 1.0 software for postprocessing. Both software packages were installed on a Dell Precision 530 with a dual 2.0 GHz Intel Xeon processor and 2 GB of RAM. IMOD is running under RedHat Linux Version 7.3 and Inspect3D is running under Windows 2000/XP.

Before tomographic reconstruction, the tilt series has to be aligned precisely with respect to a common tilt axis, thereby minimizing both blurring of small features and artifacts in the reconstruction. In IMOD this is achieved by a combination of rough cross-correlation alignment and least-squares fitting of fiducial markers such as gold nanoparticles. Typically 15–30 markers (well distributed over the imaged area) were tracked throughout the tilt series and were used as the basis to refine x–y image shifts, image rotation, and magnification (adjustment typically less than 0.1–0.5%). In some cases, the tilt angle was also refined within strict limits (less than 0.1° adjustment between successive images and less than 2° adjustment over the whole tilt series).

In the case of Inspect3D, the tilt-series alignment was done only using cross-correlations. An iterative approach has been implemented in Inspect3D; by adding the shifts measured from all iterations prior to applying them to the original data set for the final subpixel alignment, it is ensured that pixel gray values are interpolated only once. In addition, a final step to improve the position and orientation of the tilt axis is done by a manual procedure where these tilt axis parameters can be interactively adjusted until reconstruction artifacts are minimized (Weyland, 2001).

The advantage of the iterative cross-correlation alignment is that it eliminates the need for marker tracking (and

†The dose used to image the area of interest was minimized by blanking the beam between CCD exposures. The images themselves were taken at a dose of 500–10,000 e/nm^2, depending on the sample and the magnification. Tracking was done based only on the tilt series itself and therefore did not add any dose to the imaging process. Focusing was done on the area of interest every 5–10 images with a reduced exposure time, adding an additional dose of about 10–20% to the tilt series. True low-dose conditions can also be used in XPlore3D, but it was not necessary to use this option for the examples presented in this article.

the presence of markers on the sample). If no image distortions are present, this approach works very well—resulting in a subpixel accurate alignment—for relatively thin samples or if features can be selected in the (Fourier filtered) images that do not change significantly with tilt angle. However, in the case of thick samples, where the image features change drastically during tilting, the iterative cross-correlation alignment may not converge, whereas an alignment using fiducial markers (if present and visible on the sample) is still possible. Furthermore, fiducial marker tracking enables not only correction of x–y shifts and the average tilt-axis orientation, but also image rotations and magnification changes can be measured and compensated for, allowing for a more accurate image alignment in case of image distortions. In particular, this becomes important if large focus changes had to be compensated for during the data acquisition due to non-eucentricity of the imaged area or poor correction of the optimized acquisition position.‡

3D Reconstruction

After the image alignment, the 3D volume is reconstructed using weighted backprojections (Gilbert, 1972*b*). Assuming a perfect tilt-series alignment, the resolution d of the reconstructed volume is controlled by the number N of projections acquired and the diameter D of the spherical volume to be reconstructed (Crowther et al., 1970):

$$d = d_y = d_z = \pi D/N.$$

However, this assumes that the N projections are evenly distributed over $\pm 90°$. In practice, the tilt range for the acquisition is limited due to the pole piece/sample holder geometry and due to the increasing projected sample thickness. This results in a "missing wedge" of information, leading to a reduced resolution d_z parallel to the optical axis. This can be expressed by an elongation factor ε, which depends on the maximum tilt angle $\alpha_{\max}$ (Rademacher, 1988):

$$d_z = d_y \times \varepsilon$$

$$\varepsilon = \sqrt{\frac{\alpha_{\max} + \cos\alpha_{\max} \sin\alpha_{\max}}{\alpha_{\max} - \cos\alpha_{\max} \sin\alpha_{\max}}}.$$

Furthermore, for thick samples, the resolution in the tilt series itself might also be limiting the resolution of the reconstruction. In BF-TEM, the inelastic scattering in combination with the chromatic aberration of the objective lens may limit the image resolution (Grimm et al., 1997). In HAADF-STEM, the convergence angle of the probe together with the scattering in the sample result in an increasing diameter of the electron beam in thick samples.

In addition to these general considerations, there are other sample specific factors, for example, for radiation-sensitive or magnetic materials, that may limit the resolution of the tomogram even further. Radiation sensitivity and beam damage are the main limitations for electron tomography in biological applications, especially in cryoelectron tomography of frozen hydrated samples (Dubochet et al., 1988; Koster et al., 1997; Grimm et al., 1998), and it is also an important factor in some materials science applications such as zeolites.

In addition to the weighted backprojection, we also started to evaluate iterative reconstruction schemes such as the simultaneous iterative reconstruction technique (SIRT) (Gilbert, 1972*a*). Here, the reconstructed volume is reprojected at the original projection angles and these projections are compared to the original images. The difference between them is characteristic for the deficiencies of the reconstruction and can be used to modify the original reconstruction in order to improve for imperfections in the backprojection. This approach helps to reduce the effects due to the missing wedge of the acquisition (Midgley & Weyland, 2003) and results in a denoising of the 3D reconstruction.

Visualization

Visualization of the reconstructed volume is done either by volume rendering or by surface rendering using Amira Version 3.0 (TGS Software). The volume rendering was optimized by adjusting the threshold for color coding and the transparency of the different components. For the surface rendering, an initial segmentation was obtained by thresholding of the data. The noise reduction achieved with SIRT turned out to improve the initial thresholding significantly. Denoising algorithms such as median filtering or nonlinear anisotropic diffusion (Frangakis & Hegerl, 2001) also help to simplify the initial thresholding. However, we prefer SIRT, as the denoising is achieved by refinement with respect to the original images, whereas denoising of reconstructions obtained by weighted backprojection cannot retrieve the information lost due to Fourier filtering. In either case, due to the artifacts induced in the reconstruction by the missing wedge, the contours were edited manually to enhance the visualization.

Materials

Oil-Refining Catalyst #1

The commercial catalyst from Haldor Topsøe A/S is based on a highly porous alumina support material with small MoO_3 particles distributed over the surface of the support. The pore system contains macropores (>50 nm) as well as mesopores (2–50 nm). The catalyst was embedded in Struers

‡In the optimized position, an image/beam shift is used to compensate for the distance between the optical axis of the microscope and the (mechanical) rotation axis of the CompuStage.

Specifix-20 and sectioned on a RMC MT-XL to a thickness of 150 nm. Ten-nanometer gold markers were applied to the sample on the TEM grid from an aqueous solution (Department of Cell Biology, University of Utrecht) and the stabilizing detergent was cleaned off with deionized water.

BF-TEM tomography data sets were acquired on a Tecnai Sphera as described above. The microscope was operated at a nominal magnification of 25,000×, resulting in a pixel size of 0.69 nm at the specimen level; the defocus was set to -2 μm. The tilt series was acquired automatically over a tilt range of $-63°$ to $+60°$ in 1° steps.

IMOD was used to align the tilt series by cross-correlation followed by marker tracking, where refinement of the average tilt-axis orientation and refinement of the magnification were enabled during alignment. The residual error of the marker tracking was 0.9 pixels. The 3D volume was reconstructed by weighted backprojection using IMOD.

Oil-Refining Catalyst #2

The second catalyst sample is a naphtha reforming catalyst containing 1–1.5-nm Pt particles on a fine-grained alumina support. The catalyst was crushed, dispersed in ethanol, and deposited on a holey carbon support foil on a standard TEM grid. Five- and 15-nm gold markers were applied to the sample on the TEM grid from an aqueous solution (Department of Cell Biology, University of Utrecht) and the detergent was cleaned off with deionized water.

BF-TEM tomography data sets were acquired on a Tecnai Sphera as described above. The microscope was operated at a nominal magnification of 68,000×, resulting in a pixel size of 0.23 nm at the specimen level; the defocus was set to -1.5 μm. The tilt series was acquired automatically over a tilt range of $\pm 65°$ in 1° steps.

The tilt-series alignment was performed with Inspect3D by iterative cross-correlation techniques using image filters to enhance the gold markers during cross-correlation. The overall tilt-axis orientation and shift were optimized semi-automatically by minimizing reconstruction artifacts of the gold markers at various positions in the 3D volume. The reconstructed volume was binned by a factor of 2 to improve the signal-to-noise ratio (before binning, 1000 slices in the *z*-direction were calculated based on only 131 input images).

High Surface Area Hydrogen Storage Medium (HSM)

The HSM was ultramicrotomed to a nominal thickness of 200 nm. This material is an advanced Mg-Ni-based hydrogen storage alloy for use in NiMH batteries. The sample was provided courtesy of Ovonic Battery Company (Fetcenko et al., 1997, 2003). Five- and 15-nm gold markers were applied to the sample on the TEM grid from aqueous solution (Department of Cell Biology, University of Utrecht) and the detergent was cleaned off with deionized water.

BF-TEM tomography data sets were acquired on a Tecnai Sphera as described above. The microscope was operated at a nominal magnification of 29,000×, resulting in a pixel size of 0.59 nm at the specimen level; the defocus was set to -2 μm. The tilt series was acquired automatically over a tilt range of $\pm 65°$ in 1° steps.

HAADF-STEM tomography data sets were acquired on a Tecnai F20 ST using an alpha version of the XPlore3D Tomography Suite (dynamic focus not implemented at the time). Micrographs with 1024×1024 pixels were acquired at a nominal magnification of 320,000×, resulting in a pixel size of 0.27 nm at the specimen level. The tilt series was acquired automatically over a range of $\pm 72°$ in 2° steps.

IMOD was used to align the tilt series by cross-correlation followed by marker tracking, where refinement of the average tilt-axis orientation and refinement of the magnification were enabled during alignment. The residual error of the marker tracking was 0.8 pixels (TEM data set) and 0.9 pixels (STEM data set). The 3D volume was reconstructed by weighted backprojection using XPlore3D and filtered with a 3D median filter with a kernel size 3 in Amira for noise reduction.

Copper Interconnect Lines

The cross section of copper interconnect lines in an AMD CPU was prepared by FIB on a FEI DB235. The TEM lamella was thinned and polished to a thickness of 150 nm, lifted out externally, and deposited on a Quantifoil TEM grid (for details about the method. see Young et al., 1998). Prior to the tomographic imaging, the sample had been used for extensive spectrum imaging, which generated some holes in the copper due to the high beam currents used for the elemental mapping.

HAADF-STEM tomography data sets were acquired on a Tecnai F20 ST using an alpha version of the XPlore3D Tomography Suite (dynamic focus not implemented at the time). Micrographs with 2048×2048 pixels were acquired at a nominal magnification of 40,000×, resulting in a pixel size of 1.5 nm at the specimen level. The tilt series was acquired automatically over a range of $-68°$ to $+70°$ in 2° steps.

Inspect3D was used to align the tilt series by an iterative cross-correlation approach and to reconstruct the 3D volume by weighted backprojection. The reconstructed volume was visualized by surface rendering using Amira. The surfaces obtained automatically by density thresholding were edited manually to enhance the barrier layer and reduce noise prior to 3D visualization.

Flash-Memory Cell

The cross section of a flash-memory cell from TSMC was prepared by FIB on a FEI DB835. The TEM lamella was thinned to a thickness of 180 nm by the ion beam, lifted out externally, and deposited on a carbon film with pre-adsorbed 10-nm gold particles.

HAADF-STEM tomography data sets were acquired on a Tecnai F20 ST using the XPlore3D Tomography Suite. Micrographs with 1024 × 1024 pixels were acquired automatically at a nominal magnification of 160,000×, corresponding to a pixel size of 0.58 nm over a tilt range of −66° to +67° in 1° steps.

IMOD was used to align the tilt series by cross-correlation followed by marker tracking, where refinement of the average tilt-axis orientation and refinement of the magnification were enabled during alignment. The residual error of the marker tracking was 0.9 pixels. The 3D volume was reconstructed by weighted backprojection using XPlore3D and filtered using a 3D median filter with kernel size 3 in Amira for noise reduction. After binning the reconstructed volume by a factor of 2, the structure of the memory cell was visualized by surface rendering using Amira. The polysilicon surfaces obtained automatically by density thresholding were edited manually for the final visualization.

The aligned tilt series was also reconstructed using the iterative backprojection algorithm SIRT (Gilbert, 1972*a*) as implemented in an alpha version of Inspect3D 2.0. Twenty iterations were performed for the SIRT reconstruction.

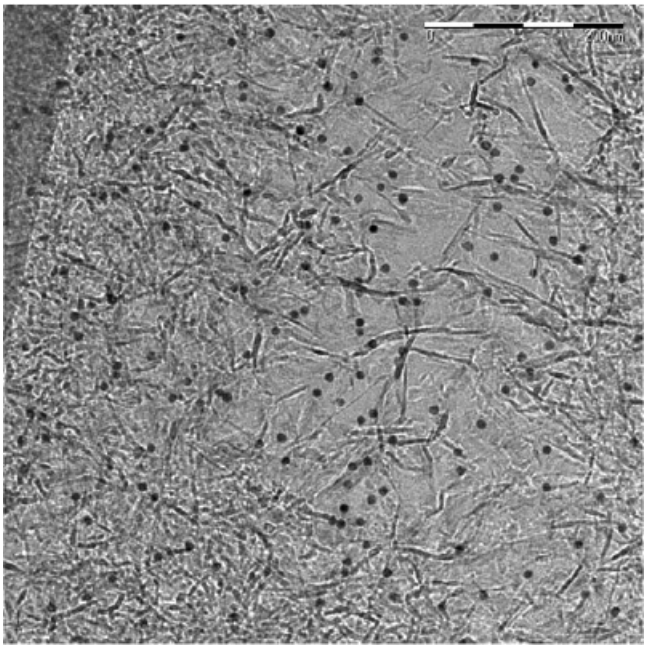

Figure 1. TEM image of a catalyst produced by Haldor Topsøe for oil refining. The projected image reveals a lower density of the support material (large pore) in the center. The larger dark particles are 10-nm gold markers used for tomography alignment later.

Results and Discussions

Catalyst Materials

Classical catalysts consist of a nanocrystalline porous support material covered by a high density of nanoparticles providing the active catalyst sites. In addition to the size and shape distribution of the active catalyst particles, the quality of a catalyst is crucially affected by the shape, pore size distribution, and permeability of the support material as well as the distribution of the active catalyst on the support material. Simple 2D projections mainly reveal information about the average density in the projected area, but the shape and pore size of the support material are difficult to interpret. Furthermore, especially for thick samples, it can be difficult to unambiguously identify the catalyst particles themselves. Figure 1 exemplifies this problem for an alumina-based oil-refining catalyst from Haldor Topsøe. The TEM projection reveals a lower density in the center of the imaged area, but it is difficult to estimate further details of the shape and size distribution of the support material, especially in the high-density areas.

In contrast, the 3D volume reconstructed by BF-TEM tomography (for details see Materials and Methods) reveals significantly more details (Figs. 2 and 3). For example, the support material has a sheetlike structure (Fig. 3) appearing as a line in the slices through the reconstructed volume. The average thickness of the sheets is 4–5 nm, but thicknesses of up to 8 nm were also observed. The sheets are observed in all orientations (within the limit of the missing wedge due to the tilt-series acquisition[§]) forming pores of different diameter and shape. In the large central pore, the support sheets are significantly more extended than the sheets found in the densely packed areas.

Based on the tomography results, it is expected that properties of the pore system, such as connectivity and tortuosity, can be determined. Because many reactions are diffusion limited, the transport properties have a great influence on the activity of the catalyst. To model and understand these transport properties, a realistic model of the pore system is needed.

The magnification used to record the data for the tomogram in Figure 2 is just high enough to recognize the actual catalyst particles. Based on Figure 2, it appears that the particles are distributed fairly uniformly. However, to reveal more details about the particle size distribution, a higher magnification would be needed.

To illustrate the characterization of the actual catalyst particles, a higher magnification tilt series has been re-

[§]Objects only exhibiting Fourier components in the missing wedge are not observed by weighted backprojection or only with reduced intensity. This means that thin sheets oriented perpendicular to the electron beam are not visible in the tomogram. A double tilt scheme, whereby two tilt series of the same area are taken with a 90° in-plane rotation between them and which are subsequently reconstructed simultaneously, would reduce the problem of the "missing wedge" to a "missing cone" (Penczek et al., 1995).

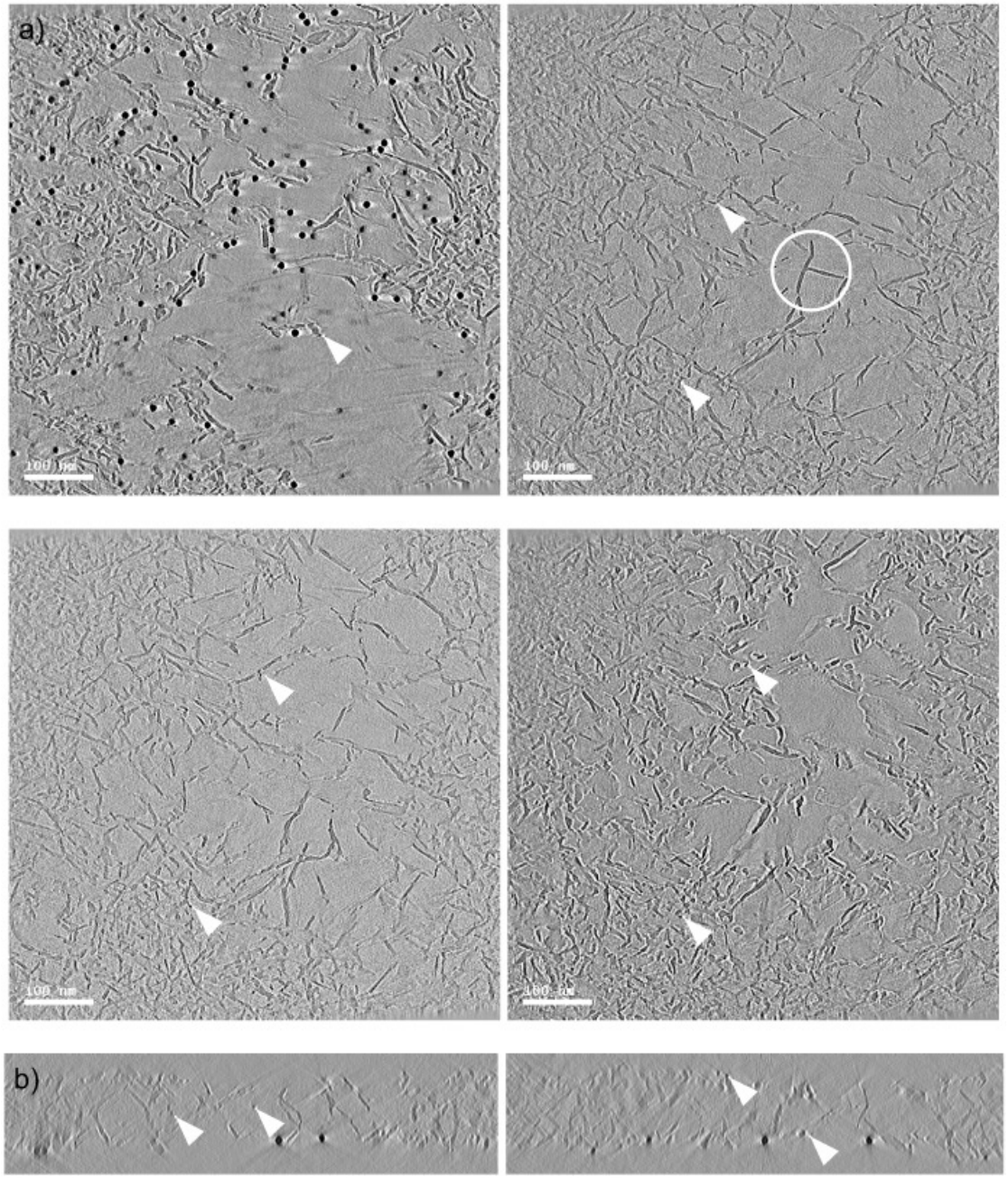

Figure 2. **a**: *x–y* slices spaced approximately 20 nm in *z* through the 3D reconstructed volume of the catalyst shown in Figure 1. In the large central pore, large sheets of the support material are predominately visible, whereas small sheets of the support material are mainly present in the dense areas. The catalyst particles themselves are also visible as small dark "spots" on the support material. The arrows indicate a few of the many catalyst particles and the circle shows the area used for surface rendering of a support sheet in Figure 3. **b**: *x–z* slices from the center and the edge of the 3D reconstructed volume of the catalyst. (A movie showing all *x–y* slices through the reconstructed volume is available as support material.)

corded for a similar catalyst (oil-refining catalyst #2). This catalyst is also based on an alumina support, but in this case the active part of the catalyst were Pt nanoparticles. Figure 4 shows a central image from the tilt series, which mainly reveals the support material as well as the gold markers used for image alignment. The active catalyst is also visible, but it is difficult to unambiguously identify the particles in a single projection of this 150-nm-thick area.

The volume reconstructed from the high-magnification tilt series shown in Figure 4 reveals the overall structure of

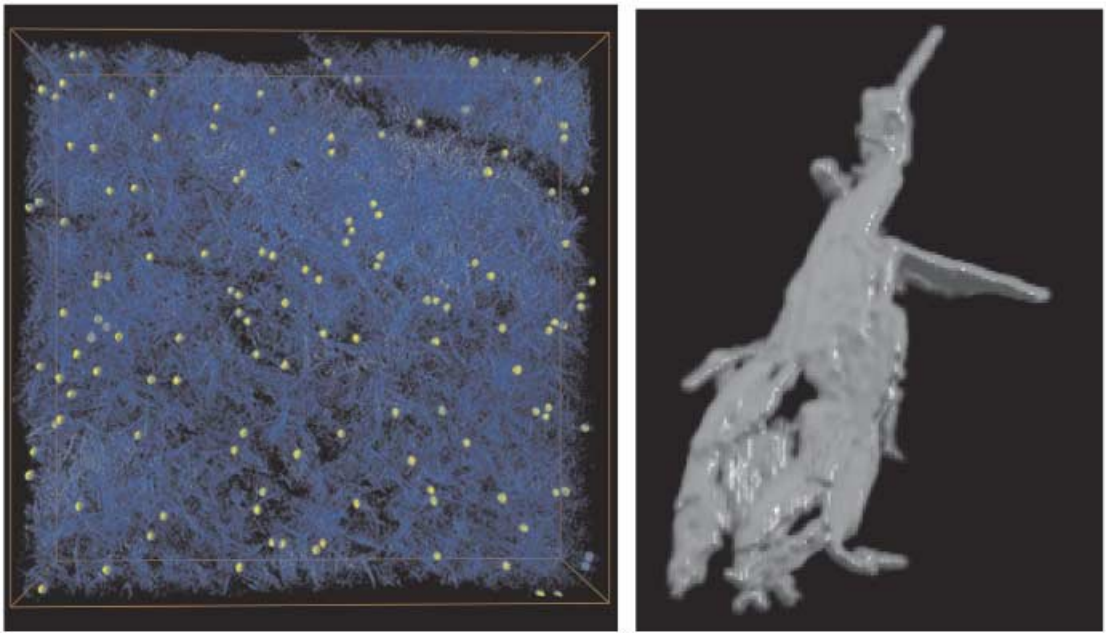

Figure 3. Volume rendering of the overall structure of the support material and surface rendering (area indicated by a white circle in Fig. 2) showing details of the sheetlike structure of the support material. (A movie showing the surface rendering of the alumina support sheet is available as supporting material.)

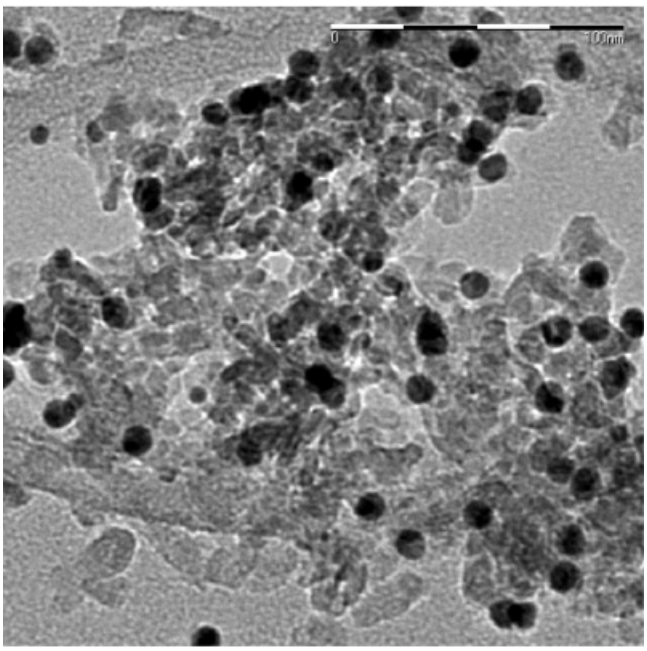

Figure 4. TEM projection of an alumina-based catalyst with Pt nanoparticles recorded at a 10° tilt. The projection reveals the support material and the gold markers used for image alignment. The active Pt-catalyst particles are also visible, but it is difficult to identify them unambiguously in the projection. (A movie showing the aligned tilt series is available as supporting material.)

the support material as well as the 3D distribution of the Pt nanoparticles (Fig. 5). The contrast in the reconstructed volume is significantly better than in the original projected images, enabling a clear identification of the Pt catalyst particles. Whereas the Pt particles are projected on top of 150 nm of alumina support in the original projections, the contrast in the reconstructed volume depends only on the density of the Pt particles compared to the alumina support.

The resolution in the reconstructed volume is not only sufficient to detect the Pt particles, but furthermore enables a statistical analysis of the size distribution. The diameter of ~40 particles in an x–y slice and 25 particles in an x–z slice through the reconstructed volume was analyzed by means of line profiles. The FWHM[¶] in the line profile was used to estimate the particle diameter (Fig. 6). The average particle diameter measured in the x–y plane is 1.7 ± 0.4 nm, whereas the average diameter measured in the z-direction is 2.1 ± 0.5 nm. The difference is as expected for the elongation of the reconstructed volume in the z-direction due to the missing wedge (Rademacher, 1988).

[¶]The tomographic reconstruction does not have an absolute intensity scale, which makes it difficult to define the zero line to estimate the FWHM in the line profiles. Therefore, the average background intensity was used as reference to estimate the FWHM.

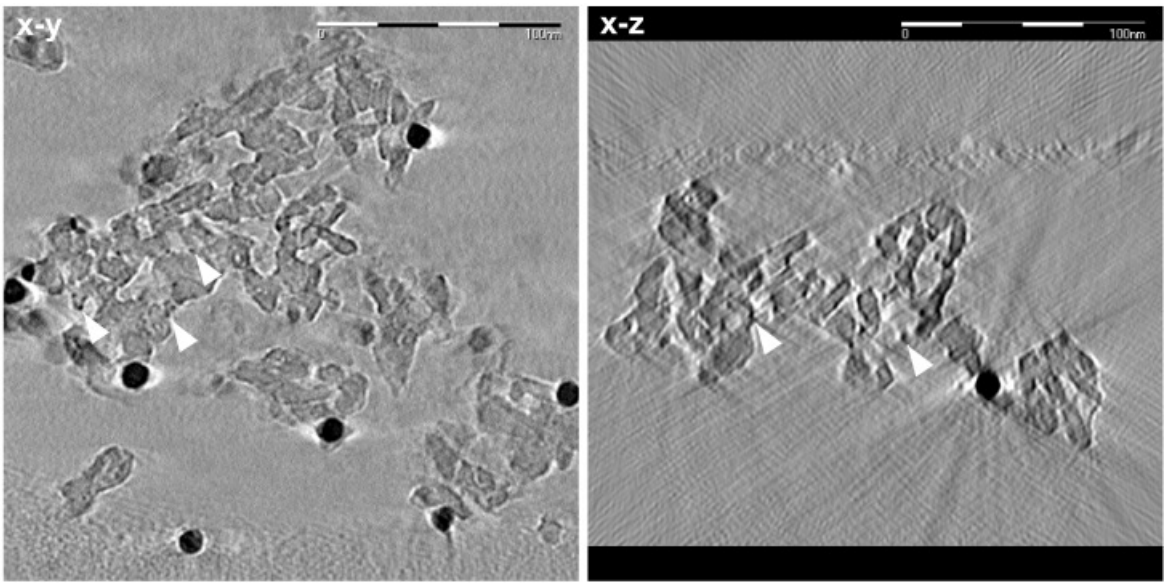

Figure 5. *x–y* and *x–z* slices through the reconstructed volume of the catalyst shown in Figure 4. The reconstruction shows the network formed by the alumina support and a large number of Pt catalyst particles (some of them indicated by arrows) as well as several large gold labels. The Pt catalyst particles can be clearly identified in the reconstructed volume due to the improved contrast in the 3D reconstruction compared to each individual 2D projection. (Movies showing all *x–y* and *x–z* slices through the reconstructed volume are available as support material.)

Overall, the particle diameter determined from the electron tomography results is slightly larger than the particle size measured by conventional HRTEM measurements in the thinnest sample areas (1.0–1.5 nm). This difference is due to the resolution of the tomogram, which may be limited by the method itself, but is also due to the pixel size of the reconstructed volume. The smallest particle diameter observed by tomography was 1.0 nm, but the number of these small particles is underestimated, shifting the measured average particle size to larger values. Nevertheless, the size distribution of particles larger than 1.5 nm will not be affected by the pixel size and reflects the true size variations.

Building on previous BF-TEM tomography results for catalysts (Koster et al., 2000; de Jong & Koster, 2002; Janssen et al., 2002, 2003; Ziese et al., 2004), the data presented here demonstrate that BF-TEM tomography is a powerful tool to analyze the 3D structure of classical catalysts despite the fact that they are crystalline. As can be seen in the tilt-series movies, the diffraction contrast in these materials is very low due to the small crystallite size and the high defect density, and, therefore, does not strongly influence the 3D reconstruction. The main advantage of TEM tomography is the short data acquisition time, allowing for collection of more data, which becomes crucial in quality control and statistical analysis.

High Surface Area Hydrogen Storage Medium

As shown in Figure 7, the HSM exhibits a complex chemical composition. EDS analysis shows the presence of nickel, magnesium, manganese, cobalt, silicon, and carbon, partially oxidized and partially as a chloride (Fig. 7). Even local 2D EDS mapping with a 1-nm probe does not reveal significant compositional variations within this sample, due to the complex 3D structure.

To gain a better understanding of the structure and morphology of the HSM, we used BF-TEM tomography. However, as the HSM contains a variety of crystals with a diameter of about 50 nm, the resulting tilt series show considerable diffraction contrast in some of the 2D projections. Nevertheless, it was possible to align the tilt series and reconstruct the 3D volume (Fig. 8) to show characteristic features of this sample.

The 3D reconstruction reveals a structured core in a HSM particle, which consists of domains with different density. Some larger (20–70 nm diameter) dense crystals and smaller (10–20 nm diameter) low-density areas are visible in the core of the particle, with the lowest density probably representing small pores in the material. In addition, a complex network of high-density platey and fibrous material is visible as well as a large number of small, dense spherical particles (3–4 nm diameter) distributed throughout the core of the HSM particle. This core is surrounded by a low-density layer with fibrils branching off. The extent of this fibrillar structure is unusually large in the example shown in Figure 8, but a layer with some fibrils branching off was observed for all HSM particles analyzed.

Even though a good idea of the overall structure can be developed based on the TEM tomography, this example also shows the limits of BF-TEM tomography for crystalline

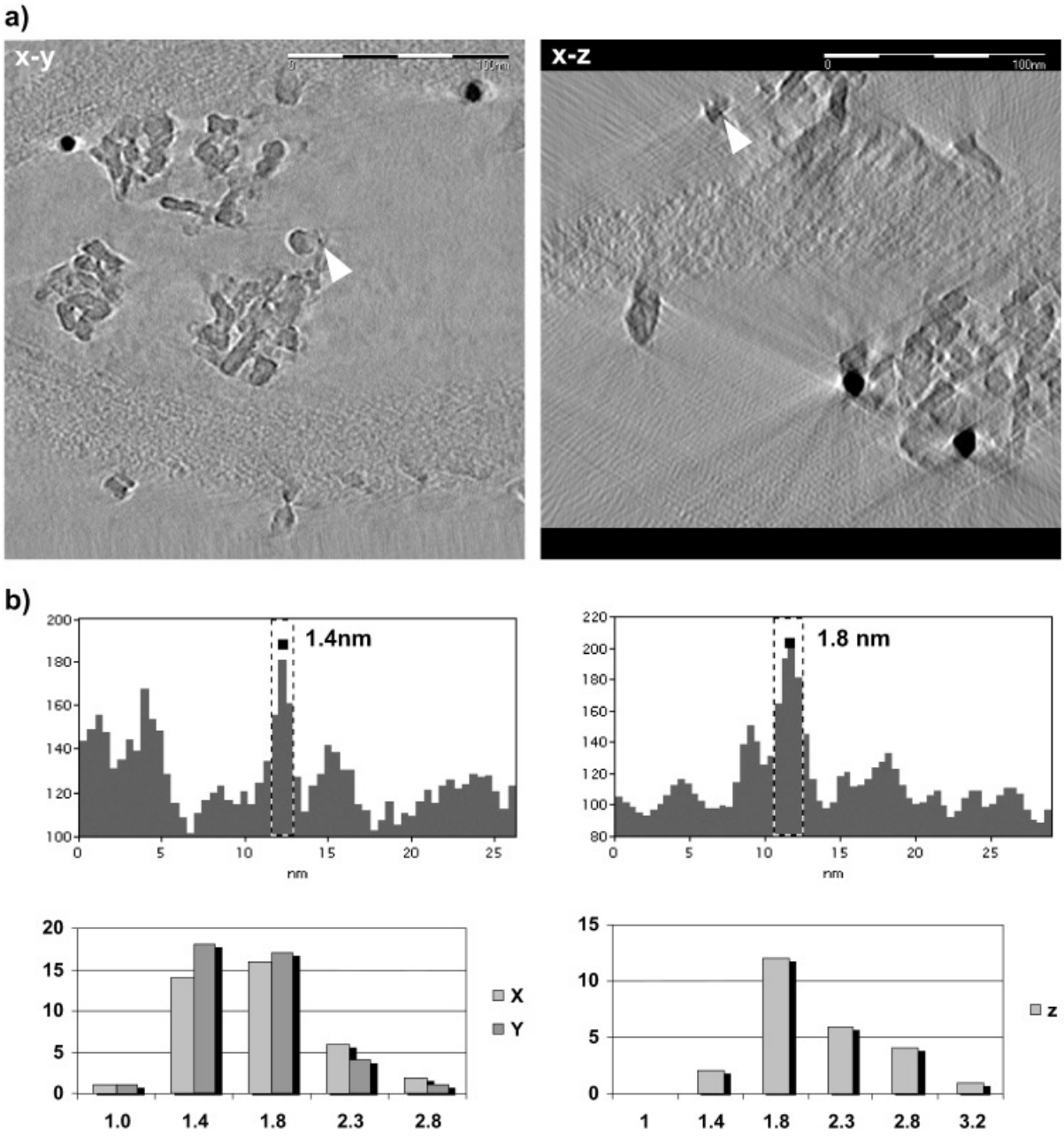

Figure 6. **a**: *x–y* and *x–z* slices through the reconstructed volume of the catalyst shown in Figure 4. The diameter of 25–40 Pt particles was analyzed by line profiles along the main directions for a statistical analysis. The FWHM of the line profile was used to estimate the particle diameter. **b**: Particle diameter distribution measured along the main directions from several slices through the reconstructed volume (**a** and Fig. 5); the values for the particle diameter in the *z*-direction are not corrected for any elongation due to the missing wedge.

materials. The 3D reconstruction reveals a clear image of the original object close to the surface of the particle where only limited diffraction contrast is observed in the tilt-series. However, in the center of the particle where several larger crystals are present, the contrast is weak, presumably due to diffraction contrast blurring the features during the backprojection.

To reduce the diffraction contribution to the images and thereby obtain a more reliable 3D reconstruction with improved contrast, we used a HAADF-STEM tilt series as the basis for the 3D reconstruction. At low camera length, no diffraction contrast was observed for the tilt series, and, furthermore, channeling contrast does not play a major role for this heterogeneous material. The 3D reconstruction

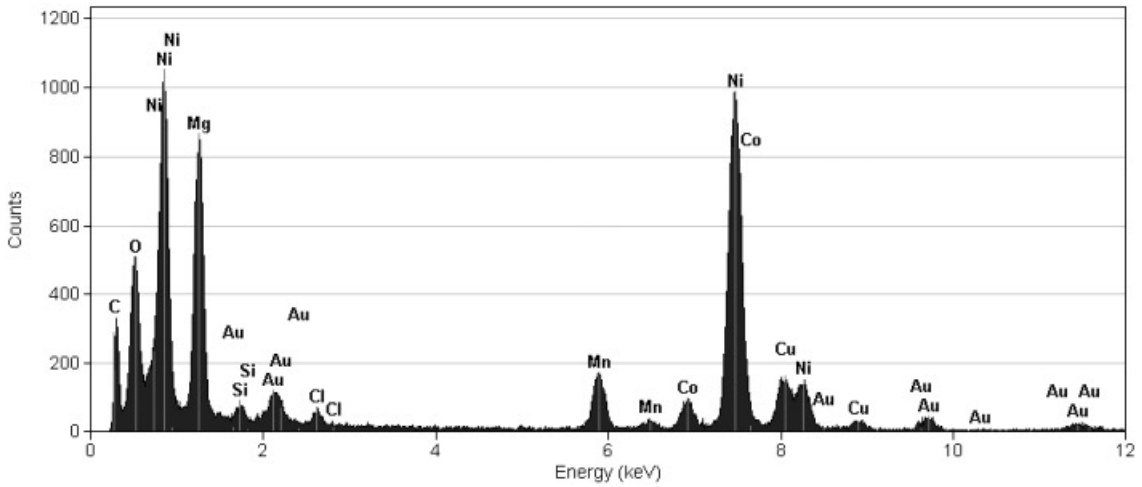

Figure 7. EDX spectrum showing the average composition of one of the HSM particles. The main elements present are nickel, magnesium, manganese, cobalt, silicon, and carbon, partially oxidized or as chloride. The gold signals are due to the gold markers applied to the sample for the tilt-series alignment.

based on the HAADF-STEM tomography tilt series (Fig. 9) shows the same basic features observed previously by BF-TEM tomography, but in this case the particle exhibited only a few fibrils branching off.

The contrast in the HAADF-STEM tomogram is significantly better than observed in the previous example due to the combined effects of reduced diffraction contrast and the different *z*-dependence in HAADF-STEM detection (Fig. 10). Therefore, identification of the different crystals within the HSM particle is easier and the high-density network can be recognized as interconnecting the large dense crystals and separating domains of low density. This distribution of the high-density material within the HSM particle is depicted by volume rendering in Figure 11. Furthermore, differences in the low-density material can also be recognized. Two different gray-level ranges can be identified for the low-density material, indicating that at least two different low-density materials are present (one of them may represent pores in the material). Even though the detailed interpretation of the density variation in terms of the elemental composition is still subject to further analysis, the tomography results give new insight into the morphology of the HSM particles and unambiguously show that there is enormous available surface area associated with the fibrous and sheetlike microstructures.

Semiconductor Devices

In the absence of large crystalline domains, BF-TEM tomography can be used to characterize the structure of semiconductor devices, for example, for seed and barrier layer analysis in (unfilled) copper lines (Stegmann & Zschech, 2002). However, in general, the use of BF-TEM tomography is limited for semiconductor devices. Typically, large crystalline grains are present, which give rise to diffraction contrast and bend contours, thereby decreasing the resolution and the contrast in the BF-TEM tomogram. In contrast, HAADF-STEM imaging exhibits only minor diffraction effects, and is, therefore, the preferred general solution for tomography in IC applications. These differences in the resulting reconstruction quality are illustrated using a transistor as an example (Fig. 12), which has been reconstructed based on a BF-TEM and a HAADF-STEM tilt series (Kübel, 2001). The TEM tomography reconstruction shows the general features of the device, but the details are blurred and it is difficult to identify individual defects. However, the contrast in the HAADF-STEM tomography reconstruction is significantly better and individual defects, such as the hole in the cobalt silicide layer and small deposits next to the transistor, can clearly be recognized (Fig. 12). For this reason, we used HAADF-STEM tomography for all further semiconductor analysis.

Copper Interconnect Lines

Interconnect structures have to be shrunk in advanced logic products to reduce the signal delay on-chip. Current devices have up to nine layers of horizontal and vertical contact lines stacked on top of the active circuit. The lines have a diameter down to about 100 nm and consist of copper and an ultrathin barrier layer (e.g., sputtered tantalum) to prevent diffusion of the copper into the active areas of the device. Important aspects of these devices are the diameter and uniformity of the barrier layer, which are difficult to estimate in a single image due to the curvature of the line. Furthermore, small voids during the electrolytic copper filling can be difficult to detect due to their low contrast in the projected image.

We have analyzed copper interconnect lines in a modern AMD CPU to evaluate the use of HAADF-STEM tomog-

a)

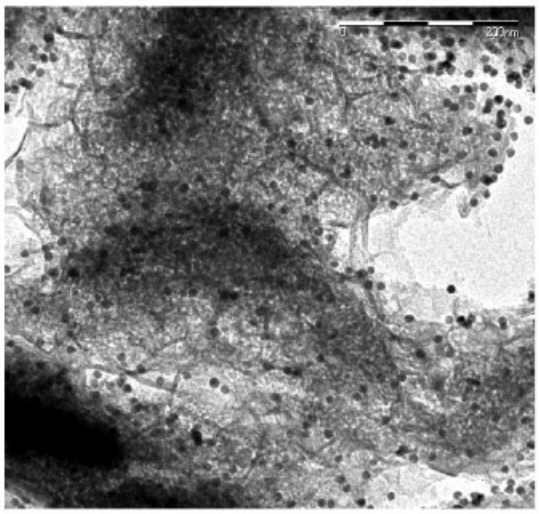

Figure 8. **a**: BF-TEM projection of a HSM particle at 0° tilt angle. The round particles visible everywhere in the projection are the gold markers applied for the tilt-series alignment. **b**: Four slices in the *x*–*y* plane of the reconstructed volume of the HSM particle. The core of the particle is highly structured, consisting of domains with different density. Some larger dense crystals and many smaller low-density areas are visible together with a complex network of high-density material. In addition, a large number of small (3–5 nm diameter) spherical particles are distributed throughout the HSM particle. This core of the particle is surrounded by a low-density layer with many fibrils branching off. (A movie showing the aligned tilt series and slices through the reconstructed volume is available as supporting material.)

b)

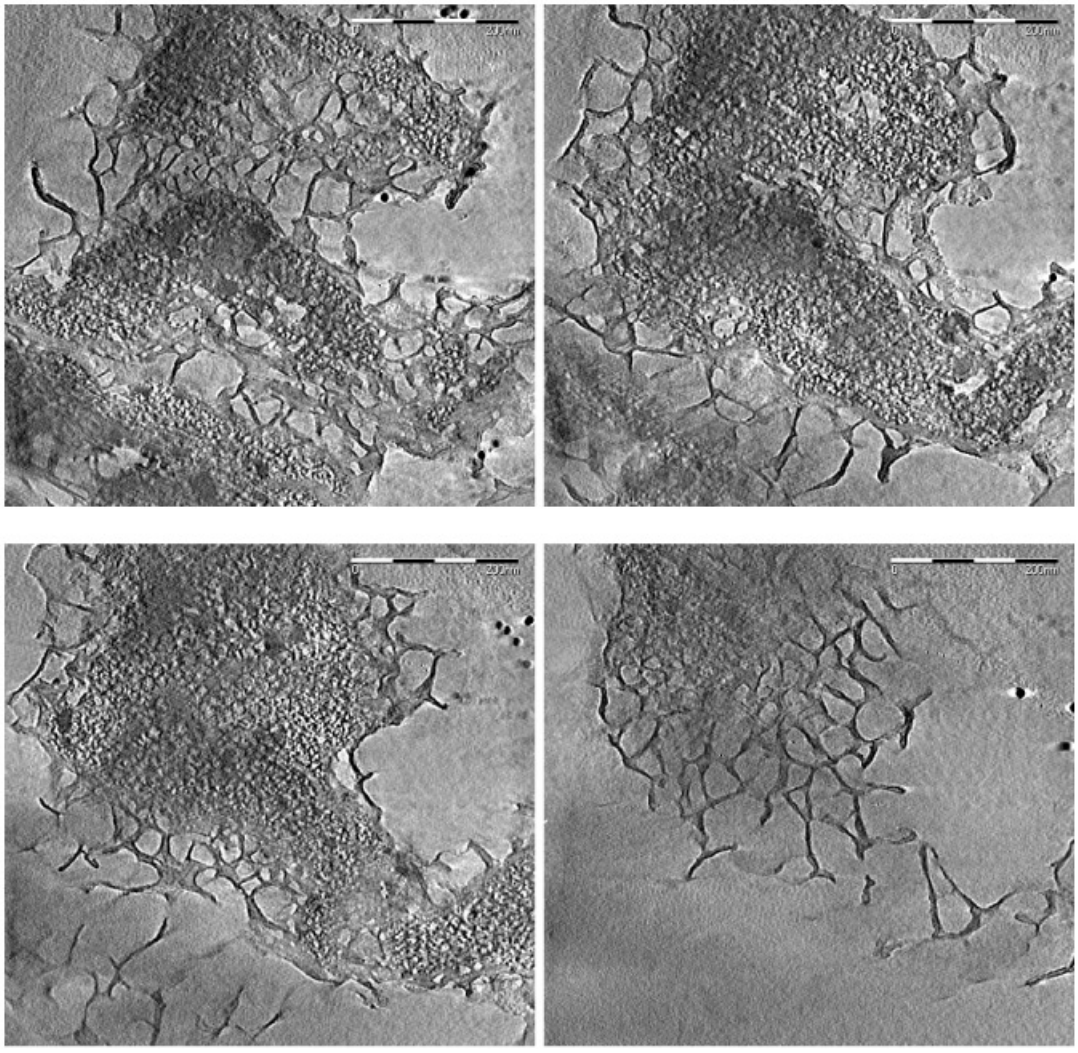

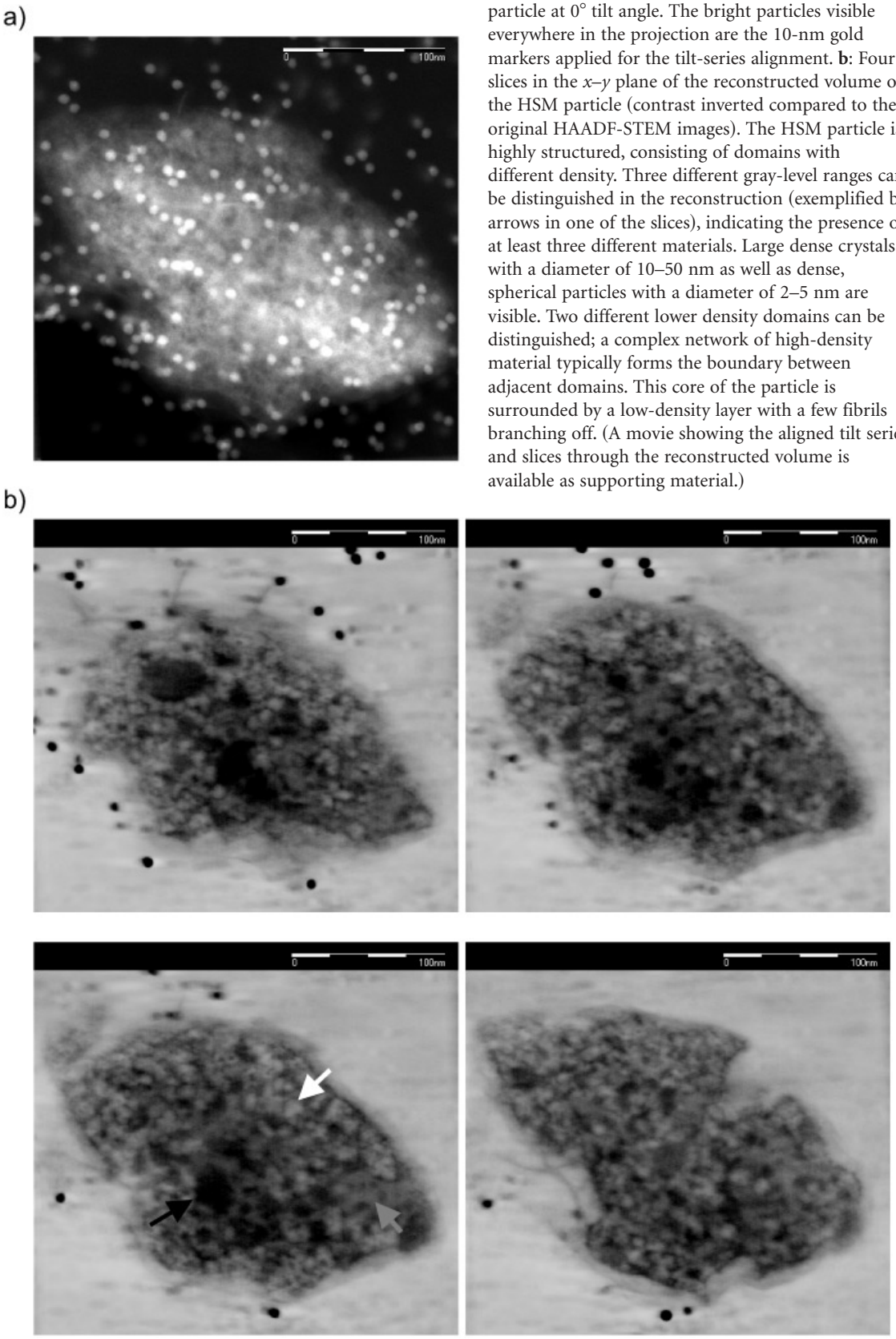

Figure 9. **a**: HAADF-STEM projection of a HSM particle at 0° tilt angle. The bright particles visible everywhere in the projection are the 10-nm gold markers applied for the tilt-series alignment. **b**: Four slices in the *x*–*y* plane of the reconstructed volume of the HSM particle (contrast inverted compared to the original HAADF-STEM images). The HSM particle is highly structured, consisting of domains with different density. Three different gray-level ranges can be distinguished in the reconstruction (exemplified by arrows in one of the slices), indicating the presence of at least three different materials. Large dense crystals with a diameter of 10–50 nm as well as dense, spherical particles with a diameter of 2–5 nm are visible. Two different lower density domains can be distinguished; a complex network of high-density material typically forms the boundary between adjacent domains. This core of the particle is surrounded by a low-density layer with a few fibrils branching off. (A movie showing the aligned tilt series and slices through the reconstructed volume is available as supporting material.)

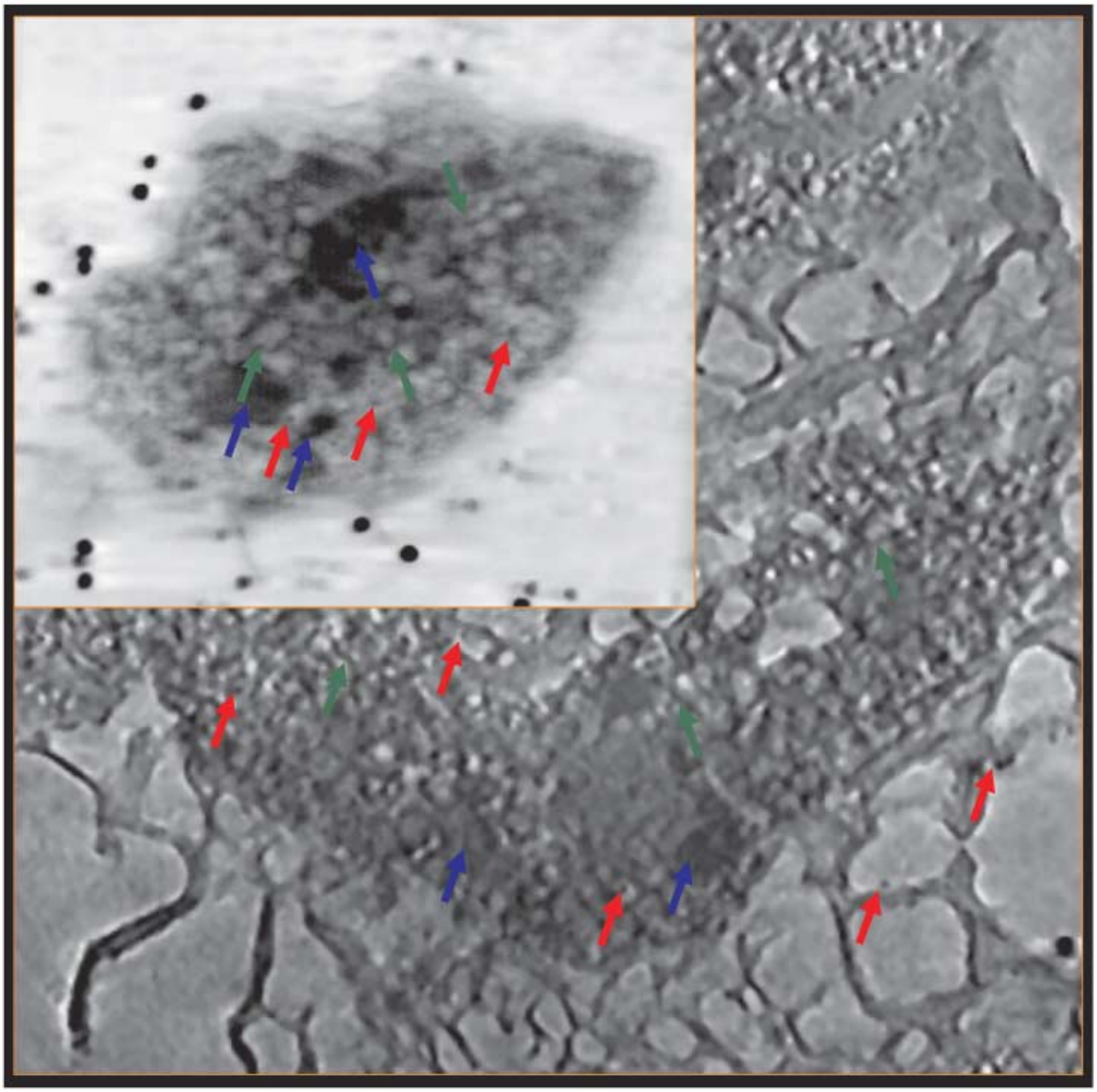

Figure 10. Comparison between the HSM particle reconstructed from BF-TEM data and a different HSM particle reconstructed from HAADF-STEM data; both particles are drawn to scale. Some of the large dense crystals (blue arrows), small spherical particles (red arrows), and the dense complex network (green arrows) are indicated in the image. Especially the large dense crystals, which exhibit significant diffraction contrast in BF-TEM, are much more visible in the HAADF-STEM reconstruction.

raphy to characterize the barrier layer and to detect small voids in the copper. To make sure that some voids were present in the area of interest, we used a sample where the electron beam had generated voids prior to the tomography analysis. The tomogram (Fig. 13) shows the barrier layer and the copper filling of several interconnect lines. The etch-stop layer is also present in the reconstructed volume, but due to the high intensity difference, it cannot be shown together with the tantalum barrier and the copper in an 8-bit gray-scale image. Overall, the barrier layer does not change significantly throughout the reconstructed volume, but a detailed analysis shows slight defects in some corners of the interconnect line, where the barrier layer thickness changes or an edge is not completely filled (indicated by circles in Fig. 13). Nevertheless, in no case did copper penetrate the barrier layer during electroplating or the following anneal steps. In addition, several small and some larger voids are visible in the copper (some are indicated by arrows in Fig. 13). The larger ones are also visible in the direct 2D projection, but the contrast in an individual projection is not sufficient to observe the smallest voids and tomography is necessary for their detection. The overall

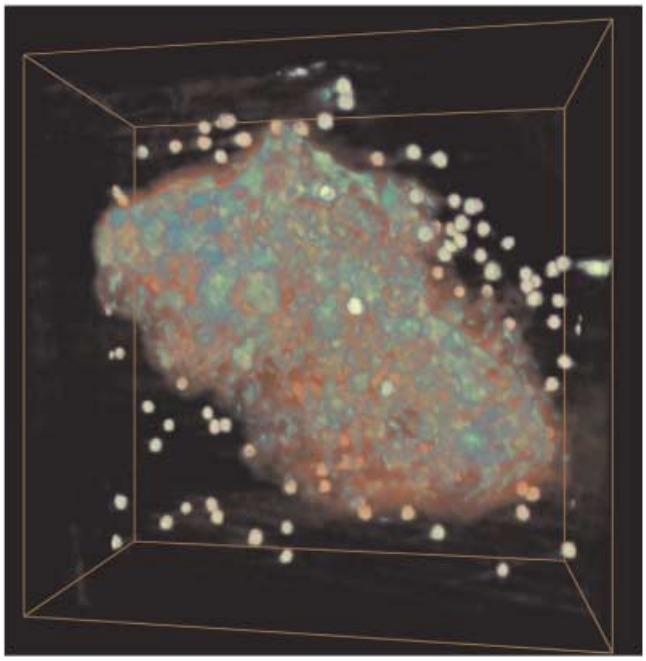

Figure 11. Volume rendering based on the HAADF-STEM tomogram showing the 3D distribution of the high-density domains (green) within a HSM particle (orange) together with the gold particles (greenish white). (A movie showing the 3D rendering from different angles is available as supporting material.)

structure of the copper interconnect lines with the barrier layer and the etch-stop layer is visualized by surface rendering in Figure 14.

Surprisingly, the copper lines show some slight structuring, which seems to coincide with the grain boundaries within the copper lines. We suspect that this is related to diffraction effects at the grain boundaries, which have not been fully suppressed at the camera length used. However, further systematic studies are needed to evaluate how the grain boundaries could be imaged in tomography.

The main limitation of the tomographic reconstruction are artifacts caused by the limited angular sampling and the missing wedge resulting in a faint "ghost" image of bright and dark lines parallel to the actual interconnect lines. Similar artifacts are presumably present in all tomographic reconstructions, but in the case of HAADF-STEM tomography of sharp, highly regular structures with strong density differences, they become particularly obvious as the intensity of the tantalum barrier layer is roughly a factor of 50 higher than the intensity of the dielectric material in the surrounding background, thereby enhancing any artifacts.

Flash-Memory Cell

Determining and controlling the roughness of interfaces in integrated circuits is becoming increasingly challenging with shrinking device dimensions. In state-of-the-art transistors, gate oxides have already reached a thickness below 2 nm and their surface roughness needs to be characterized and controlled almost at the atomic level. This is beyond the resolution of current electron tomography techniques, but it is possible to image interfaces with nanometer resolution to detect, for instance, spikes resulting in a short circuit. This is illustrated using the analysis of a flash-memory cell by HAADF-STEM tomography as an example.

Figure 15 shows a HAADF-STEM image acquired at 0° of a flash-memory cell produced by TSMC. The image shows the overall structure of the memory cell with the floating gate and the reference gate as the main components. In the 2D projection, a beacon is visible on the floating gate pointing toward the reference gate. This beacon exhibits intensity variations only hinting at a nonuniform structure within the depth of the sample. After 3D reconstruction, the HAADF-STEM tomogram reveals significantly more details about the roughness and shape of the floating and reference gates. Four slices in the x–y plane of the reconstructed volume are shown in Figure 16. They reveal the changing shape of the floating gate throughout the thickness of the sample. At one position, no beacon is observed, whereas, at a different height, the beacon of the floating gate is almost in contact with the reference gate. The observed structural changes are most pronounced at the beacon of the floating gate, but some surface roughness is observed in other areas, for example, on top of the floating gate. The overall structure of the device and the surface roughness of the floating gate is depicted by surface rendering in Figure 17.

Even though the reconstructed volume shown in Figure 16 reveals significant details about the shape and roughness of the device structure, the weighted backprojection suffers from two problems: First, the 3D reconstruction exhibits considerable noise, which makes automatic identification of the different components difficult. Second, the sharp interface with the tungsten via on the left side of the reconstruction leads to similar artifacts as previously observed in the 3D reconstruction of the copper vias, which appear as bright lines in the reconstructed volume. However, as the low-Z material is of interest in this case, the artifacts appear more prominently.

A promising approach to reduce the noise and also the missing-wedge related artifacts in the reconstruction are iterative algorithms. Figure 18 shows slices through the volume reconstructed by 20 iterations with SIRT based on the same aligned tilt series as used for the weighted backprojection in Figure 16. The overall features observed in the volume reconstructed with SIRT are almost the same as observed in the weighted backprojection except for small differences in the roughness of the floating gate. However, the noise is significantly reduced, thereby enabling a much clearer identification of the materials' contrast due to the atomic number (density) differences. The poly-silicon gate structure, the different silicon oxide capping layers, and the interlayer dielectrics exhibit clear gray scale differences even

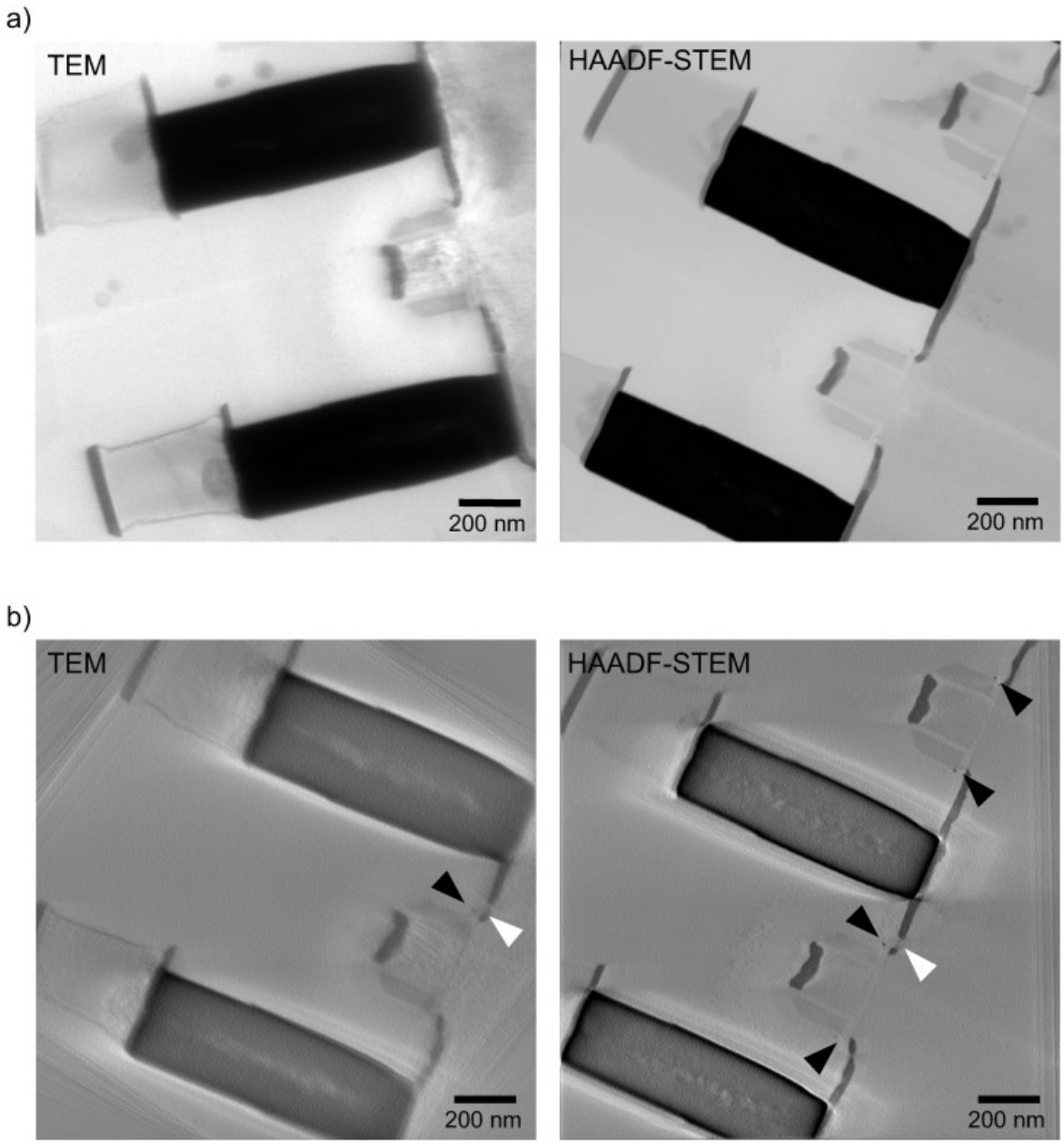

Figure 12. **a**: BF-TEM and (inverted) HAADF-STEM image of a transistor and tungsten contacts. The BF-TEM image exhibits strong diffraction contrast and bend contours, which are greatly reduced by HAADF-STEM imaging. **b**: 3D reconstruction based on the BF-TEM and (inverted) HAADF-STEM tilt series. The images show a slice in the x–y plane through the reconstructed volume at the same position in the sample. The acquisition geometry and the alignment quality were identical in both cases, but the HAADF-STEM results show significantly more and much clearer details compared to the BF-TEM tomography data. The HAADF-STEM tomogram reveals, for instance, a hole in the cobalt silicide layer (indicated by the white arrow) and several small deposits next to the transistor (indicated by the black arrows).

in the presence of the tungsten via and titanium silicide on top of the reference gate (Fig. 19). However, it is not possible to differentiate between polysilicon and silicon nitride, as both materials exhibited the same scattering strength in the original HAADF-STEM tilt-series images. Interestingly, in most areas, the poly-silicon exhibits a sharp interface with the surrounding oxide. However, some small domains with gray levels intermediate between silicon and silicon oxide are observed, raising the question of whether a different chemical composition is present there (circled area in Fig. 19). Some artifacts due to the edge of the tungsten via are still present in the SIRT reconstruction and these

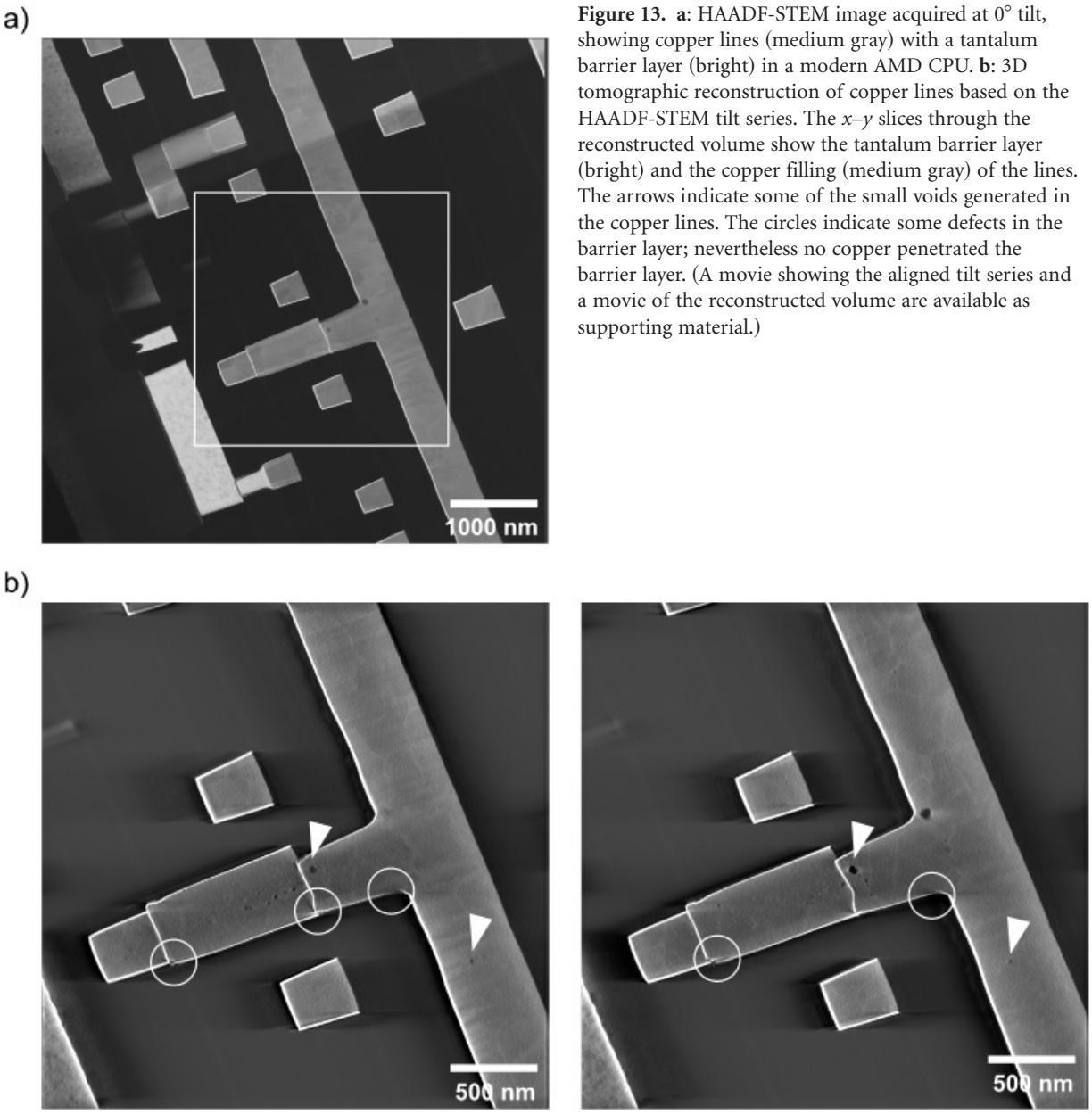

Figure 13. **a**: HAADF-STEM image acquired at 0° tilt, showing copper lines (medium gray) with a tantalum barrier layer (bright) in a modern AMD CPU. **b**: 3D tomographic reconstruction of copper lines based on the HAADF-STEM tilt series. The *x*–*y* slices through the reconstructed volume show the tantalum barrier layer (bright) and the copper filling (medium gray) of the lines. The arrows indicate some of the small voids generated in the copper lines. The circles indicate some defects in the barrier layer; nevertheless no copper penetrated the barrier layer. (A movie showing the aligned tilt series and a movie of the reconstructed volume are available as supporting material.)

cause intensity variations in the reconstructed volume. However, in the area indicated in Figure 19, this does not appear to be the reason for the intensity variations observed at the beacon.

Conclusion

Both BF-TEM and HAADF-STEM imaging have some advantages and disadvantages for tomography. For example, TEM image acquisition and the auto-focus are significantly faster (25–40 min) compared to STEM mode (45–90 min). On the other hand, by using the dynamic focus option in STEM tomography, it is possible to compensate for the tilt-induced differences in sample height, which otherwise result in defocus differences across the image in TEM tomography. Therefore, we expect that STEM tomography will ultimately result in a higher resolution than conventional TEM tomography. Another consideration is the different *Z*-dependence, which scales approximately with $Z^{3/4}$ for BF-TEM compared to $Z^{\sim 1.7}$ for HAADF-STEM imaging. Thus, if the structure of low-*Z* materials is to be imaged in the presence of high-*Z* materials, BF-TEM tomography will make better use of the dynamic range of the imaging device, whereas HAADF-STEM tomography is best suited to visualize high-*Z* materials (in a light matrix). For example, 1-nm Pd-Ru particles could be imaged in a mesoporous

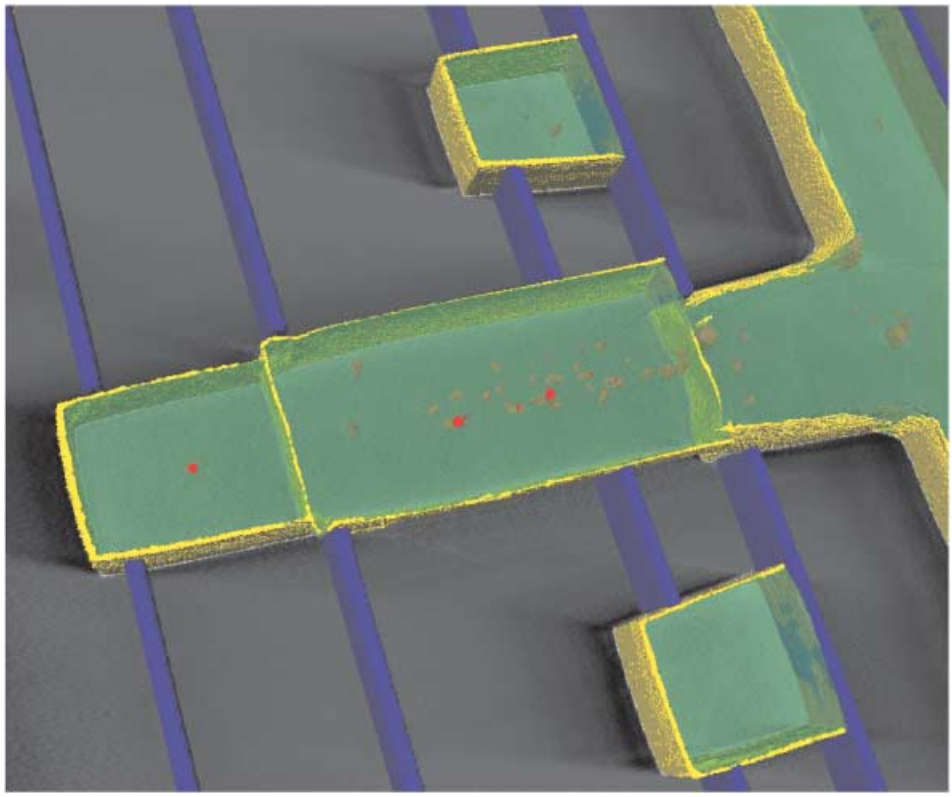

Figure 14. Surface rendering based on the HAADF-STEM tomogram showing the 3D structure of the interconnect lines with some bending and slight variations of the tantalum barrier layer (yellow). The copper is depicted green and the 3D distribution of the voids within the copper is shown in red. The etch-stop layer is depicted blue. (A movie showing the 3D rendering from different angles is available as supporting material.)

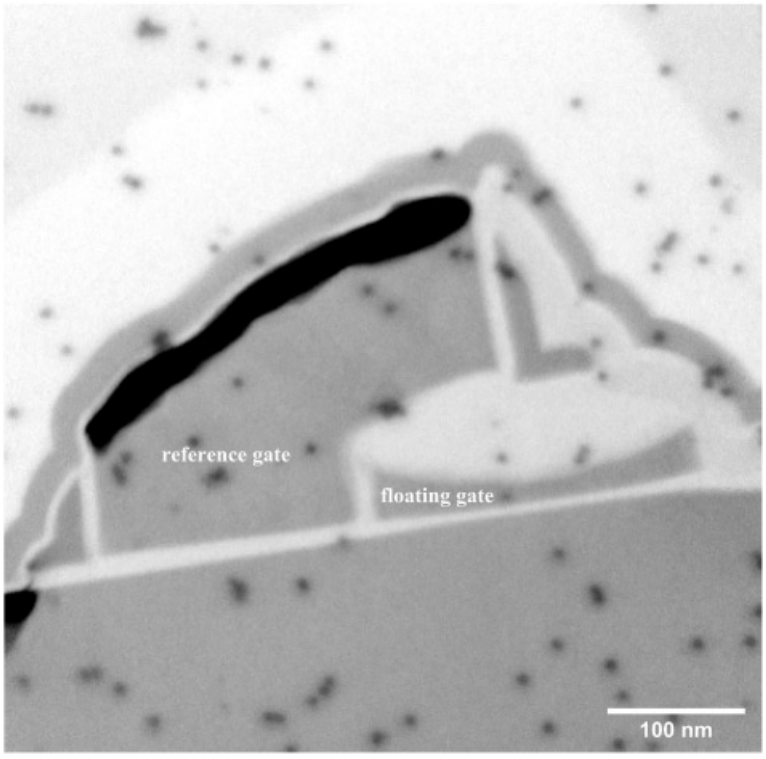

Figure 15. HAADF-STEM image of a flash-memory cell produced by TSMC (contrast inverted). The image shows the floating and the reference gate of the memory cell as the main components of the storage device. Furthermore, a large number of gold markers are visible, which were used for alignment of the tilt series. (A movie showing the aligned tilt series and a movie of the reconstructed volume are available as supporting material.)

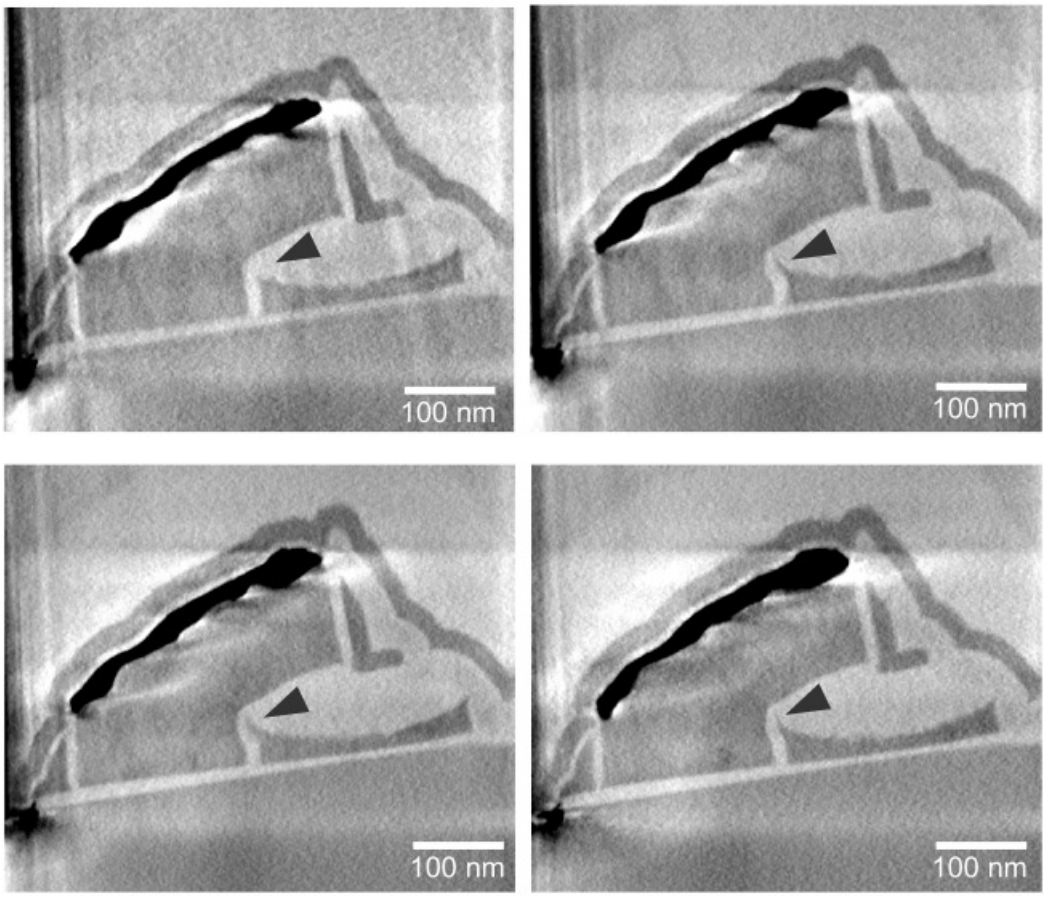

Figure 16. 3D tomographic reconstruction of a flash-memory cell based on an (inverted) HAADF-STEM tilt series. The *x*–*y* slices through the reconstructed volume show the poly-silicon floating gate and the reference gate on top of the silicon waver as the main components of the storage device. In addition, the edge of the tungsten via is visible on the left side. The 3D reconstruction reveals the changing shape of the floating gate, especially the shape of the beacon pointing toward the reference gate (indicated by a black arrow). Furthermore, the surface roughness on the top side of the floating gate is visible in these slices. (A movie showing the aligned tilt series and a movie of the reconstructed volume are available as supporting material.)

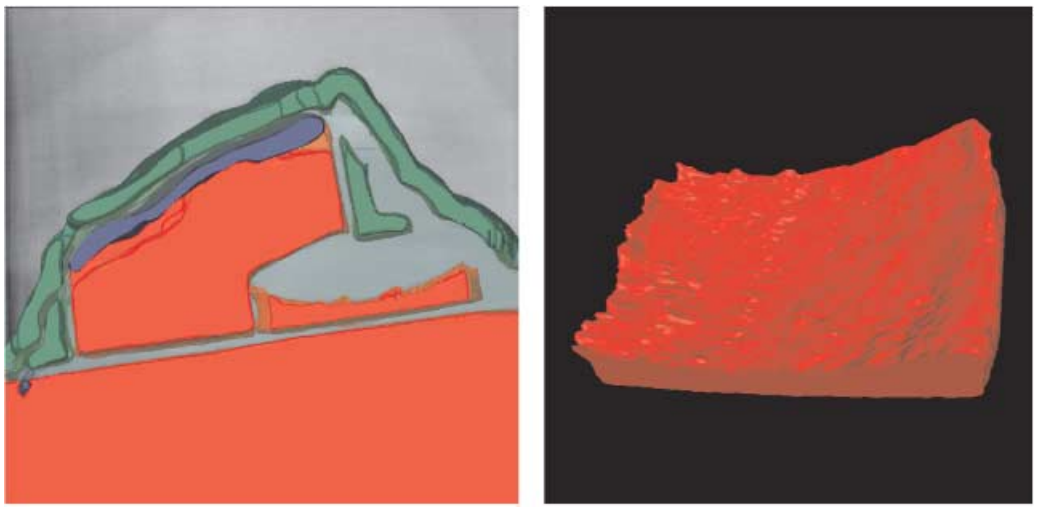

Figure 17. **a**: Surface rendering showing the overall 3D structure of the memory cell based on the volume obtained by weighted backprojection (silicon: red, silicon nitride: green, titanium silicide: blue). **b**: Surface rendering of the floating gate showing the roughness at the top of the floating gate based on the SIRT reconstruction (Fig. 18).

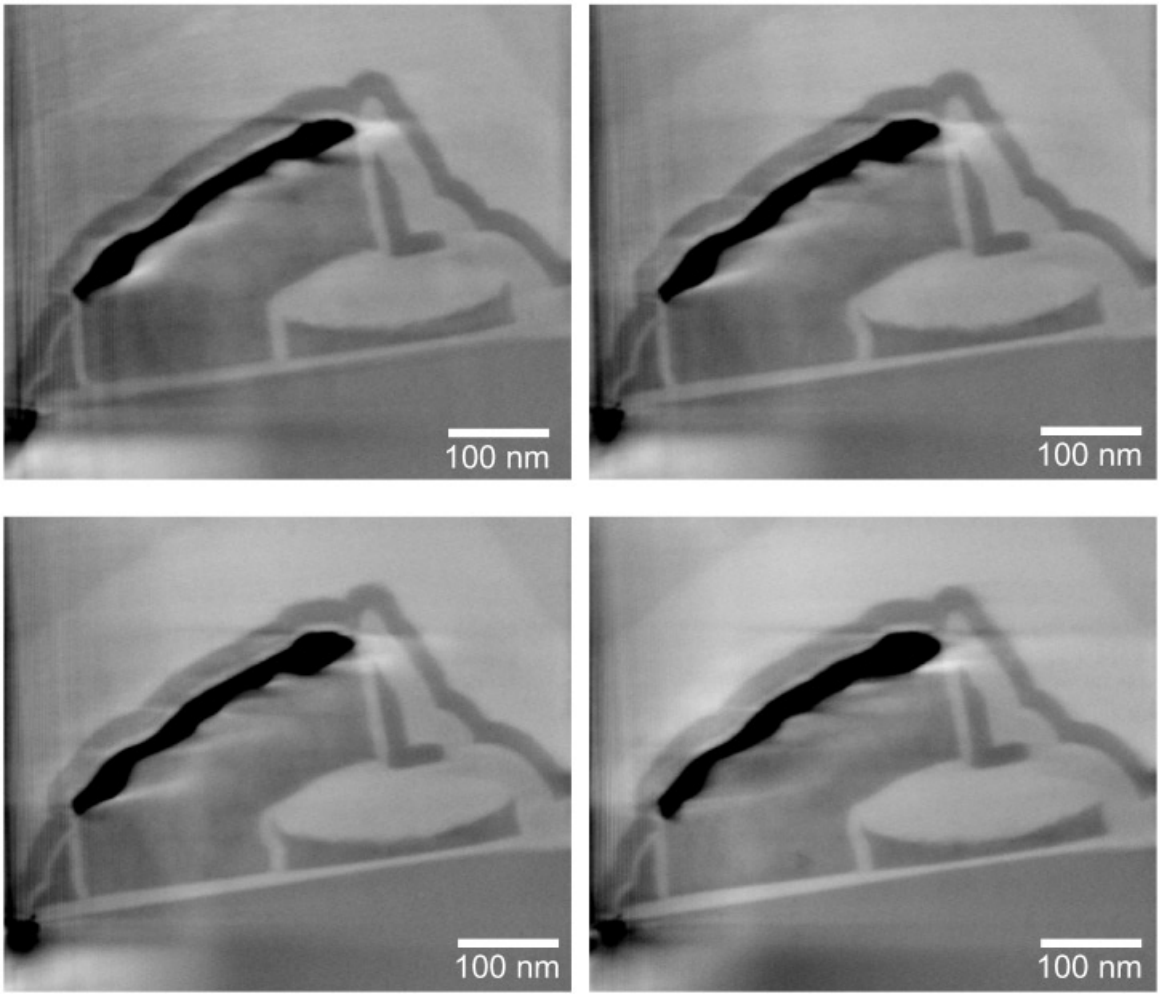

Figure 18. 3D tomographic reconstruction using a SIRT algorithm with the same aligned tilt series as used in Figure 16. Slices in the *x*–*y* plane of the reconstruction are shown approximately at the same position as in Figure 16. In principle, the volume reconstruction with SIRT shows the same features as the volume obtained by weighted backprojection, except for some small differences in the roughness of the floating gate. However, the noise in the reconstruction is significantly lower, enabling a clearer detection of the atomic number contrast between the different parts of the device. (A movie showing the aligned tilt series and a movie of the reconstructed volume are available as supporting material.)

silica (Midgley et al., 2001; Midgley & Weyland, 2003) and the location of 0.8-nm nano gold markers on hair cell stereocilia (Ziese et al., 2002*b*) could be visualized by HAADF-STEM tomography.

Despite these arguments, the most crucial difference between BF-TEM and HAADF-STEM tomography is the ability to work with highly crystalline materials by using HAADF-STEM imaging. The examples in this article and previous work (de Jong & Koster, 2002; Janssen et al., 2002, 2003; Ziese et al., 2004) show that some diffraction contrast can be tolerated in BF-TEM tomography, meaning that, for example, most catalysts can probably be imaged by TEM tomography. However, as the crystallite size or the crystal density within the sample increase, BF-TEM tomography becomes more limited. Crystals with a diameter of about 50 nm already induce noticeable blurring in the 3D reconstruction of the HSM and larger crystalline domains, as encountered in the transistor, prevent any reliable 3D reconstruction. In contrast, HAADF-STEM tomography was not noticeably limited by diffraction contrast or channeling effects. Even in the case of highly crystalline samples such as the copper lines or the flash-memory cell, HAADF-STEM tomography provided 3D information not obtainable by any other method for these materials.

Some artifacts are present in the 3D reconstructions due to the limited angular sampling and the missing wedge during data acquisition. These artifacts are particularly visible in 3D reconstructions of semiconductor devices due to their strong density differences and sharp interfaces in the devices. However, the iterative reconstruction algorithm

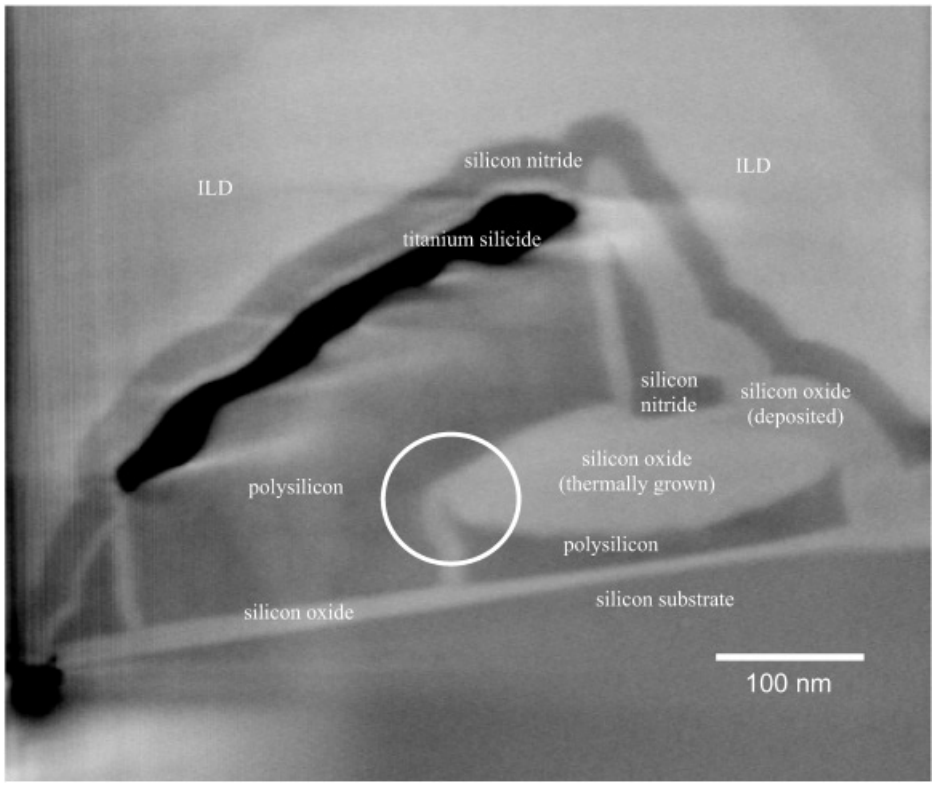

Figure 19. The volume reconstructed by SIRT reveals clear gray-level differences due to differences in density and chemical composition, thus enabling observation of the thermally grown and deposited silicon oxide as well as the interlayer dielectric (ILD). The small scattering strength differences of the silicon oxides can be visualized even though the dynamic range of the HAADF-STEM detector was optimized to cover the full intensity range of the heavy elements titanium silicide and tungsten. However, it is not possible to differentiate between polysilicon and silicon nitride, as both materials also appear the same in the original HAADF-STEM images.

SIRT slightly reduces these artifacts and significantly reduces the noise in the reconstructed volume, which is an important step toward easier identification of materials within the reconstructed volume.

By using both BF-TEM and HAADF-STEM tomography in materials science, features with dimensions on the order of 2 to 3 nm can be observed on a routine basis even for medium-thick samples of 150–200 nm. In addition, even below the 2-nm level, it is possible to measure size distributions accurately down to a diameter of at least 1.5 nm and detect particles with a diameter of 1 nm. With this resolution, electron tomography has the potential to help provide answers to a wide range of characterization challenges in the physical sciences.

Acknowledgments

The authors would like to thank Dr. Hans-Jürgen Engelmann (AMD) for his support on engineering of copper VIAs and Anne-Mette Heie Kjær for TEM sample preparation of the catalyst #1. The authors are grateful to Dr. Jennifer Kübel for editing the manuscript.

References

Anderson, M.W., Ohsuna, T., Sakamoto, Y., Liu, Z., Carlsson, A. & Terasaki, O. (2004). Modern microscopy methods for the structural study of porous materials. *Chem Comm* **8**, 907–916.

Batson, P.E. (1999). Advanced spatially resolved EELS in the STEM. *Ultramicroscopy* **78**, 33–42.

Baumeister, W., Grimm, R. & Walz, J. (1999). Electron tomography of molecules and cells. *Trends Cell Biol* **9**, 81–85.

Breysse, M., Afanasiev, P., Geantet, P. & Vrinat, M. (2003). Overview of support effects in hydrotreating catalysts. *Catal Today* **86**, 5–16.

Browning, N.D. & Pennycook, S.J. (2000). *Characterization of High T_C Materials and Devices by Electron Microscopy*. Cambridge, UK: Cambridge University Press.

Buseck, P.R., Dunin-Borkowski, R.E., Devouard, B., Frankel, R.B., McCartney, M.R., Midgley, P.A., Pósfai, M. & Weyland, M. (2001). Magnetite morphology and life on Mars. *Proc Natl Acad Sci USA* **99**, 13490–13495.

Crowther, R.A., de Rosier, D.J. & Klug, A. (1970). The reconstruction of a three-dimensional structure from projections and its application to electron microscopy. *Proc R Soc London A* **317**, 319–340.

Datye, A.K. (2003). Electron microscopy of catalysts: Recent achievements and future prospects. *J Catal* **216**, 144–154.

Dubochet, J., Adrian, M., Chang, J.-J., Homo, J.-C., Lepault, J., McDowall, A.W. & Schultz, P. (1988). Cryo-electron microscopy of vitrified specimens. *Quart Rev Biophys* **21**, 129–228.

de Jong, K.P. & Koster, A.J. (2002). Three-dimensional electron microscopy of mesoporous materials—Recent strides towards spatial imaging at the nanometer scale. *Chem Phys Chem* **3**, 776.

Dhar, G.M., Srinivas, B.N., Rana, M.S., Kumar, M. & Maity, S.K. (2003). Mixed oxide supported hydrodesulfurization catalysts—A review. *Catal Today* **86**, 45–60.

Fetcenko, M.A., Ovshinsky, S.R., Reichman, B., Young, K., Chao, B. & Im, J. (1997). United States Patent 5,616,432.

Fetcenko, M.A., Ovshinsky, S.R., Reichman, B., Young, K., Chao, B. & Im, J. (2003). United States Patent Pending 10/733,702.

Frangakis, A.S. & Hegerl, R. (2001). Noise reduction on electron tomographic reconstructions using nonlinear anisotropic diffusion. *J Struct Biol* **135**, 239–250.

Frank, J. (1992). *Electron Tomography: Three-dimensional Imaging with the Transmission Electron Microscope*. New York: Plenum Press.

Gilbert, P. (1972*a*). Iterative methods for the three-dimensional reconstruction of an object from projections. *J Theor Biol* **36**, 105–117.

Gilbert, P.F.C. (1972*b*). The reconstruction of a three-dimensional structure from projections and its application to electron microscopy. II Direct methods. *Proc Roy Soc London B* **182**, 89–102.

Grimm, R., Bärmann, M., Häckl, W., Typke, D., Sackmann, E. & Baumeister, W. (1997). Energy filtered electron tomography of ice-embedded actin and vesicles. *Biophys J* **72**, 482–489.

Grimm, R., Singh, H., Rachel, R., Typke, D., Zillig, W. & Baumeister, W. (1998). Electron tomography of ice-embedded prokaryotic cells. *Biophys J* **74**, 1031–1042.

James, E.M. & Browning, N.D. (1999). Practical aspects of atomic resolution imaging and analysis in STEM. *Ultramicroscopy* **78**, 125–139.

Janssen, A.H., Koster, A.J. & de Jong, K.P. (2001). Three-dimensional transmission electron microscopic observations of mesopores in dealuminated zeolite Y. *Angew Chem Int Ed Engl* **40**, 1102–1104.

Janssen, A.H., Koster, A.J. & de Jong, K.P. (2002). A three-dimensional transmission electron microscopic study combined with texture analysis. *J Phys Chem B* **106**, 11905–11909.

Janssen, A.H., Yang, C.M., Wang, Y., Schüth, F., Koster, A.F. & de Jong, K.P. (2003). Localization of metal (oxide) particles in SBA-15 using bright-field electron tomography. *J Phys Chem B* **107**, 10552–10556.

Jia, C.L., Lentzen, M. & Urban, K. (2003). Atomic-resolution imaging of oxygen in Perovskite ceramics. *Science* **299**, 870–873.

Kisielowski, C., Hetherington, C.J.D., Wang, Y.C., Kilaas, R., O'Keefe, M.A. & Thust, A. (2001). Imaging columns of the light elements carbon, nitrogen and oxygen with sub Ångstrom resolution. *Ultramicroscopy* **80**, 243–263.

Koster, A.J., Grimm, R., Typke, D., Hegerl, R., Stoschek, A., Walz, J. & Baumeister, W. (1997). Perspectives of molecular and cellular electron tomography. *J Struct Biol* **120**, 276–308.

Koster, A.J. & Klumperman, J. (2003). Electron microscopy in cell biology: Integrating structure und function. *Suppl Nat Rev Cell Biol* **2003**, SS6–SS10.

Koster, A.J., van den Bos, A. & van der Mast, K.D. (1987). An autofocus method for a TEM. *Ultramicroscopy* **21**, 209–221.

Koster, A.J., Ziese, U., Verkleij, A.J., Janssen, A.H. & De Jong, K.P. (2000). Three-dimensional electron microscopy: A novel imaging and characterization technique with nanometer scale resolution for materials science. *J Phys Chem B* **104**, 9368–9370.

Kübel, C. (2001). Application of electron tomography for materials science. Tomography Workshop of the Koninklijke Nederlandse Akademie van Wetenschappen, Amsterdam.

Lee, T.-C., Huang, J.-Y., Chen, L.-C., Hwang, R.-L. & Su, D. (2002). Methodology for TEM analysis of barrier profiles. ISTFA Conference, 2002.

McEwen, B.F. & Marko, M. (2001). The emergence of electron tomography as an important tool for investigating cellular ultrastructure. *J Histochem Cytochem* **49**, 553–563.

McIntosh, J.R. (2001). Electron microscopy of cells: A new beginning for a new century. *J Cell Biol* **153**, F25–F32.

Midgley, P.A. & Weyland, M. (2003). 3D electron microscopy in the physical sciences: The development of Z-contrast and EFTEM tomography. *Ultramicroscopy* **96**, 413–431.

Midgley, P.A., Weyland, M., Thomas, J.M. & Johnson, B.F.G. (2001). Z-contrast tomography: A technique in three-dimensional nanostructural analysis based on Rutherford scattering. *Chem Comm* **18**, 907–908.

Möbus, G., Doole, R.C. & Inkson, B.J. (2003). Spectroscopic electron tomography. *Ultramicroscopy* **96**, 433–451.

Muller, D.A., Sorsch, T., Moccio, S., Baumann, F.H., Evans-Lutterodt, K. & Timp, G. (1999). The electronic structure at the atomic scale of ultrathin gate oxides. *Nature* **399**, 758–761.

Penczek, P., Marko, M., Buttle, K. & Frank, J. (1995). Double-tilt electron tomography. *Ultramicroscopy* **60**, 393–410.

Rademacher, M. (1988). 3-dimensional reconstruction of single particles from random and nonrandom tilt-series. *J Electron Microsc Technol* **9**, 359–394.

Sali, A., Glaeser, R., Earnest, T. & Baumeister, W. (2003). From words to literature in structural proteomics. *Nature* **422**, 216–225.

Spence, J. (2002). Achieving atomic resolution. *Materials Today* **5**, 20–33.

Stegmann, H. & Zschech, E. (2002). Electron tomography of semiconductor copper interconnect structures. *G.I.T. Imaging & Microscopy* **4**, 8–9.

Voyles, P.M., Muller, D.A., Grazul, J.L., Citrin, P.H. & Gossmann, H.-J.L. (2002). Atomic-scale imaging of individual dopant atoms and clusters in highly *n*-type Si. *Nature* **416**, 826.

Weyland, M. (2001). Two and Three Dimensional Nanoscale Analysis: New Techniques and Applications. Ph.D. Thesis, Cambridge, UK.

Weyland, M. (2002). Electron tomography of catalysts. *Top Catal* **21**, 175–183.

Weyland, M. & Midgley, P.A. (2003). Extending energy-filtered transmission electron microscopy (EFTEM) into three dimensions using electron tomography. *Microsc Microanal* **9**, 542–555.

Weyland, M., Midgley, P.A. & Thomas, J.M. (2001). Electron tomography of nanoparticle catalysts on porous supports: A new technique based on Rutherford scattering. *J Phys Chem* **B105**, 7882–7886.

Young, R.J., Carleson, P.D., Da, X., Hunt, T. & Walker, J.F. (1998). High-yield high-throughput TEM sample preparation using focus ion beam automation. *Proceedings of the 24th*

International Symposium for Testing and Failure Analysis, ISTFA 98, pp. 329–336. Materials Park, Ohio: ASM International.

Ziese, U., de Jong, K.P. & Koster, A.J. (2004). Electron tomography: A tool for 3D structural probing of heterogeneous catalysts at the nanometer scale. *Appl Catal A: Gen* 260, 71–74.

Ziese, U., Janssen, A.H., Murk, J.L., Geerts, W.J., Van der Krift, T., Verkleij, A.J. & Koster, A.J. (2002*a*). Automated high-throughput electron tomography by pre-calibration of image shifts. *J Microsc* **205**, 187–200.

Ziese, U., Kübel, C., Verkleij, A.J. & Koster, A.J. (2002*b*). Three-dimensional localization of ultra-small immuno-gold labels by HAADF-STEM tomography. *J Struct Biol* **138**, 58–62.

Zschech, E., Engelmann, H.-J., Stegmann, H., Saage, H. & de Robillard, Q. (2003). Barrier/seed step coverage analysis in via structures for inlaid copper process control. *Future Fab Intl* **14**.